Part One

Nonlinear Vibrational Spectroscopy

Chapter 1

Water Hydrogen Bonding Dynamics at Charged Interfaces Observed with Ultrafast Nonlinear Vibrational Spectroscopy

Emily E. Fenn and Michael D. Fayer
Department of Chemistry, Stanford University, Stanford, California

1.1 INTRODUCTION

The question of how charged species affect water structure and dynamics is relevant to many applications in chemistry, biology, geology, and industry. Biological systems are often crowded aqueous environments filled with proteins, membranes, vesicles, and other structures that often rely on the presence of ions for stability and proper functioning [1–6]. The ion–water interface is critical for ion exchange resins [7, 8], heterogeneous catalysis [9–11], electrochemistry [12], as well as processes involving mineral dissolution [13, 14] and ion adsorption [15, 16]. Because the behavior of water in the presence of ions impacts a wide range of technical and scientific fields, a great deal of literature over the years has been dedicated to studying the aqueous solvation of ions and the properties of water at charged interfaces. Studies that have examined ion–water interfaces have employed *x*-ray and neutron diffraction [17–19], Raman spectroscopy [20], ultrafast infrared spectroscopy [21–26], Fourier transform

Vibrational Spectroscopy at Electrified Interfaces, First Edition.
Edited by Andrzej Wieckowski, Carol Korzeniewski, and Björn Braunschweig.

infrared (FTIR) spectroscopy [20, 27], and other spectroscopic techniques [15, 28, 29]. Theoretical models [30, 31], molecular dynamics (MD) simulations [32–35], and Monte Carlo (MC) calculations [20] have also been employed. While simulations can provide some insight into the underlying dynamics, most experimental techniques only provide steady-state data. Here we utilize ultrafast infrared spectroscopy to examine the hydrogen bonding dynamics of water at several types of charged and uncharged interfaces.

Ultrafast infrared spectroscopy has been shown to be a powerful technique for elucidating dynamics in water–ion systems [21–26], other hydrogen bonding systems [36–43], protein environments [44–52], and systems that undergo chemical exchange [25, 53–57]. Here, we apply ultrafast infrared pump–probe and two-dimensional infrared (2D IR) vibrational echo spectroscopic techniques to examine the dynamics of water when it is confined in nanoscopic environments and interacting with interfaces. The question is whether the nature of confinement or the chemical composition of the interface most significantly influences the dynamics. To explore this question, the dynamics of water at charged and neutral interfaces in reverse micelles are compared. In addition, water in ionic solutions is investigated. Some water molecules are hydrogen bonded to ions, while others are hydrogen bonded to water molecules. These are in equilibrium, with water molecules bound to ions switching and becoming bound to water molecules, and vice versa. Using 2D IR chemical exchange spectroscopy, we determine the exchange time required for a water hydroxyl initially hydrogen bonded to an anion to switch to being hydrogen bonded to another water molecule.

Reverse micelles consist of a water pool surrounded by a layer of surfactant molecules and are often used as model systems for confined environments. The surfactant molecules are terminated by a hydrophilic head group that can be either charged or neutral. These hydrophilic head groups face in toward the water pool while the alkyl (hydrophobic) tails of the surfactant are suspended in a nonpolar organic phase. A schematic of a reverse micelle utilizing the surfactant Aerosol-OT, or AOT [sodium bis(2-ethylhexyl) sulfosuccinate], is shown in Figure 1.1. The AOT surfactant (Fig. 1.2) forms spherical monodispersed reverse micelles that have been well characterized. The size of the AOT reverse micelles can be easily controlled by varying the amounts of starting materials according to the w_0 parameter: $w_0 = [H_2O]/[\text{surfactant}]$ [58–60]. AOT can yield sizes of $w_0 = 0$ (essentially dry reverse micelles) all the way up to $w_0 = 60$, which has a water pool diameter of 28 nm and contains ~350,000 water molecules [61]. Isooctane is a common solvent used as the nonpolar phase of AOT reverse micelle systems, but other solvents such as carbon tetrachloride, cyclohexane, and benzene can also be used with minimal changes in water pool size for a given w_0 [62]. A recent study has shown that the identity of the nonpolar phase has no effect on the water pool dynamics [63].

As shown in Figure 1.2, AOT has a sulfonate head group with a sodium counterion. The head group region of the reverse micelle therefore creates a charged interface that surrounds the water pool. The sodium ions will generally reside in a region close to the interface. Figure 1.1 illustrates the regions of a reverse micelle. When the total water pool diameter, d, is sufficiently large (≥4.6 nm) the reverse

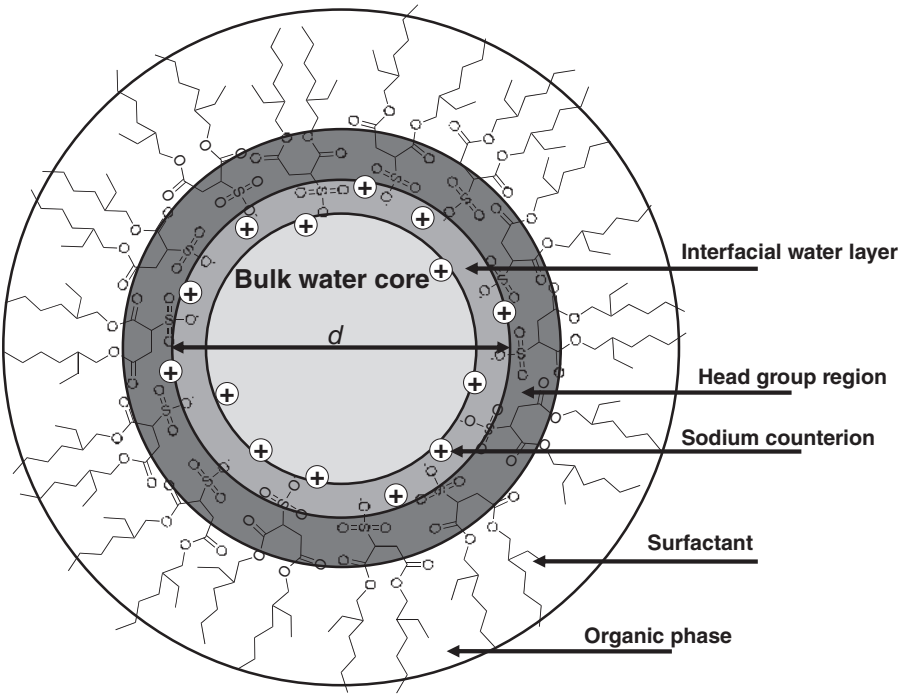

Figure 1.1 Illustration of the reverse micelle interior. The bulk water core is surrounded by a layer of interfacial water. The total water pool diameter is denoted by *d*. The hydrophilic AOT head groups face in toward the water pool while the alkyl tails are suspended in the organic phase. The sodium counterions are dispersed in the water pool, but they generally reside close to the head group interface.

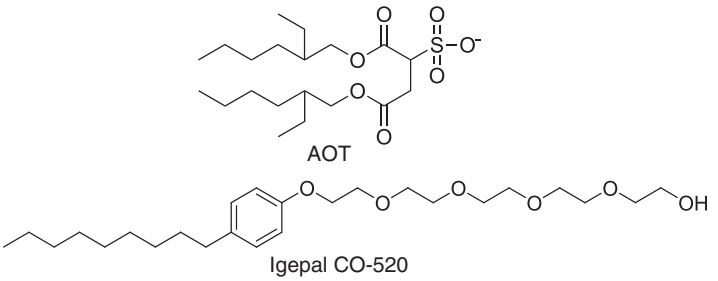

Figure 1.2 Molecular structures for AOT and Igepal CO-520. AOT (top) is terminated by a charged sulfonate head group with a sodium counterion while Igepal (bottom) has a neutral hydroxyl head group.

micelle can support a core of water with bulklike properties. Below we will discuss how far perturbations from the charged sulfonate interfacial region extend into the water pool and what happens to the water dynamics as the size of the water pool changes in size. The chemical identity of the surfactant layer can be changed by using a neutral surfactant molecule called Igepal CO-520 (Fig. 1.2). Igepal is terminated with neutral hydroxyl head groups, so the interfacial water molecules will be exposed to a very different chemical surface compared to the AOT reverse micelle system. To what extent changes in surfactant identity, particularly charged versus neutral head group regions, and reverse micelle size affect water dynamics will be described.

Water dynamics are investigated through the processes of orientational relaxation, spectral diffusion, and vibrational relaxation, which can be measured with ultrafast infrared vibrational spectroscopy. These observables report on how the hydrogen bond network of water evolves and rearranges over time. The hydroxyl stretch of water is monitored during the experiments and is used as a reporter for hydrogen bond dynamics. During vibrational relaxation, vibrational energy dissipates by transferring into a combination of low-frequency modes, such as torsions and bath modes [64, 65]. Energy must be conserved during this process. Certain pathways that facilitate vibrational relaxation in one system may or not be present in a different system. Thus, vibrational relaxation is extremely sensitive to local environments. Orientational relaxation measures how quickly water molecules reorient by monitoring the direction of the transition dipole of the hydroxyl stretch. Molecular reorientation is involved in water hydrogen bond exchange, which leads to global hydrogen bond network reorganization [66, 67]. Bulk water consists of an extended network of hydrogen bonds that are continually rearranging and exchanging with one another. According to the theory of Laage and Hynes, water molecules exchange hydrogen bonds via a jump reorientation mechanism that involves concerted motions of water molecules in the first and second solvation shells [66, 67]. The mechanism proceeds when a molecule in the second solvation shell of another water molecule moves in toward the first solvation shell. In order to swap hydrogen bonds with the approaching water from the second solvation shell, a water molecule must pass through a five-coordinate transition state and then undergo a large-amplitude rotational motion (or "jump"). The jump allows it to switch one of its hydrogen bonds to the approaching water molecule. These large-amplitude jumps change the orientation of the transition dipole. Solutes and interfaces (such as the surfactant shell of the reverse micelles) can disrupt the jump reorientation mechanism, thus slowing down the process of reorientation [23, 68–72]. Both vibrational and orientational relaxation can be measured with ultrafast infrared pump–probe spectroscopy.

Ultrafast 2D IR vibrational echo spectroscopy is used to measure spectral diffusion of the water hydroxyl stretch. The linear infrared absorption spectrum of the hydroxyl stretch is very broad due to a large distribution in the lengths and strengths of hydrogen bonds. At the beginning of the 2D IR experiment, a hydroxyl will vibrate at a certain frequency, but due to dynamic structural evolution of the system, that frequency will change over time. This process of frequency evolution is known

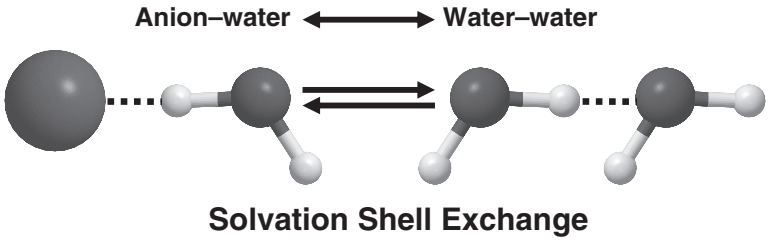

Figure 1.3 Representation of solvation shell exchange. The time it takes for a water hydroxyl initially hydrogen bonded to an anion (left side) to switch to being hydrogen bonded to another water hydroxyl (right side) can be measured with 2D IR vibrational echo spectroscopy.

as spectral diffusion and reports on how quickly water molecules sample different structural environments.

In addition, 2D IR vibrational echo chemical exchange spectroscopy is used to examine how quickly a water hydroxyl bound to an anion will switch to being hydrogen bonded to a neighboring water hydroxyl. This process is illustrated schematically in Figure 1.3. A model system for studying water–ion exchange is a solution of sodium tetrafluoroborate ($NaBF_4$) in water because the linear IR absorption spectrum of the solution yields two resolved peaks corresponding to waters interacting with other waters and waters interacting with the tetrafluoroborate anions. It is found that the ion–water hydrogen bond switching time is ~7 ps [25]. This switching time has implications when treating the orientational relaxation dynamics of water molecules inside reverse micelles made of charged and neutral surfactants [71]. Together, these ultrafast infrared experiments involving water in reverse micelles and water–ion chemical exchange construct a dynamic picture of the behavior of water molecules at charged interfaces and interacting with ions.

1.2 EXPERIMENTAL METHODS

1.2.1 Sample Preparation

Carbon tetrachloride (CCl_4), cyclohexane, isooctane, H_2O, D_2O, AOT, Igepal CO-520, and $NaBF_4$ were used as received. Stock solutions of 0.5 M AOT were prepared in CCl_4, cyclohexane, and isooctane. A variety of solvents are necessary due to certain experimental considerations that will be discussed below. A 0.3-M stock solution of Igepal CO-520 was prepared in cyclohexane. The residual water contents of the stock solutions were measured via Karl Fischer titration. The reverse micelle samples were prepared by mass by adding appropriate amounts of a solution of 5% HOD (water with one hydrogen exchanged with deuterium) in H_2O to measured quantities of the AOT or Igepal stock solutions to obtain the desired w_0. In the ultrafast experiments, the OD stretch of 5% HOD in H_2O is probed because it not only provides an isolated stretching mode to interrogate but also prevents vibrational excitation transfer processes from artificially causing decay of the orientational correlation function and observables related to spectral diffusion [73, 74]. MD simulations demonstrate that

a dilute amount of HOD does not perturb the structure and properties of H_2O and that the OD stretch reports on the dynamics of water [75].

For the pump–probe experiments involving large reverse micelles presented here, the 0.5-M stock solution of AOT in isooctane was used to make samples of $w_0 = 10$, 16.5, 25, 37, and 46 (diameters of 4.0, 5.8, 9, 17, and 20 nm, respectively). It has been found that the combination of AOT and isooctane causes distortions in vibrational echo experiments, so for vibrational echo experiments on small reverse micelles the 0.5-M AOT/CCl_4 stock solution was used to make $w_0 = 2$, 4, and 7.5 (diameters of 1.7, 2.3, and 3.3 nm, respectively) [63]. CCl_4 cannot support reverse micelles larger than $w_0 \sim 10$ [61], so the 0.5-M AOT/cyclohexane stock solution was used to make $w_0 = 12$ and 16.5 (diameters of 4.6 and 5.8 nm, respectively) for vibrational echo experiments on larger reverse micelles. Neither CCl_4 nor cyclohexane cause distortions in the vibrational echo experiments. Cyclohexane can only reliably make reverse micelles of $w_0 < 20$ [76, 77], so the vibrational echo studies are limited to the lower bound of large sizes. It will be shown that both $w_0 = 12$ and 16.5 have well-defined bulk water cores and interfacial water regions, so analysis of these sizes should provide insight into the behaviors of water molecules in the even larger sizes.

To compare the effects of the chemical composition of the interface, Igepal reverse micelles with $w_0 = 12$ and 20 were also made. Like AOT, Igepal also makes monodispersed spherical reverse micelles [78]. The AOT and Igepal surfactants have different aggregation numbers, thus yielding different sizes for the same w_0 values. The $w_0 = 12$ Igepal reverse micelles have the same 5.8-nm diameter as AOT $w_0 = 16.5$ while the $w_0 = 20$ reverse micelles have the same 9-nm diameter as AOT $w_0 = 25$. AOT lamellar structures (sheets of AOT surfactants with water between them) were prepared by adding water to dry AOT to produce samples with various water-to-surfactant ratios, λ. These lamellar samples allow us to examine the effects of confining geometry on the water dynamics (spherical confinement versus confinement within layers).

The experimental samples are contained between two calcium fluoride windows that are separated by a Teflon spacer. The thickness of the Teflon spacer is chosen such that the optical density of the OD stretch region is ~0.1 for the vibrational echo experiments and ~0.5–0.7 for the pump–probe experiments.

For the 2D IR chemical exchange experiments, a 5.5-M solution of $NaBF_4$ in water was used. Again, the water component consisted of 5% HOD in H_2O for the same reasons outlined above. The 5.5-M concentration corresponds to a system with seven water molecules per $NaBF_4$ molecule ($n = 7$). For linear IR absorption measurements, additional samples of 1.7 M, 3.1 M, and 4.3 M of $NaBF_4$ in water were made, corresponding to $n = 30$, 15, and 10, respectively.

1.2.2 2D IR Vibrational Echo Spectroscopy

The laser system used to generate the infrared light that excites the OD hydroxyl stretch consists of a Ti–sapphire oscillator that seeds a regenerative amplifier. The

output of the regenerative amplifier pumps an optical parametric amplifier that generates near-infrared wavelengths that are difference frequency mixed in a $AgGaS_2$ crystal. The resulting mid-IR pulses are centered at ~4 μm (2500 cm^{-1}) but can be tuned to the peak of the absorption spectrum for a given sample (e.g., 2565 cm^{-1} for $w_0 = 2$ AOT reverse micelle). The generated mid-IR beam enters a 2D IR vibrational spectrometer that can be readily converted into a pump–probe setup.

The pump–probe and 2D IR vibrational echo techniques presented here are noncollinear four-wave mixing experiments [79, 80]. In these experiments, three field–matter interactions between the sample and the incident ultrafast laser pulses create a third-order macroscopic polarization that emits a signal electric field. Depending upon the type of experiment, the signal electric field carries different types of information. As discussed in the introduction, the signal from a pump–probe experiment allows one to extract vibrational lifetimes and orientational relaxation parameters for the OD stretch of HOD in H_2O. The vibrational lifetime and orientational observables are sensitive to local structural and chemical environments. 2D IR vibrational echo spectroscopy is a sophisticated technique that observes how vibrational chromophores in a system evolve in frequency over time via chemical exchange, spectral diffusion, coherence transfer, or other processes. 2D IR spectroscopy can monitor these frequency changes by manipulating the quantum pathways by which the system evolves.

The experimental pulse sequence for the 2D IR vibrational echo experiments is shown in Figure 1.4*a*. The pump–probe experiment (Fig. 1.4*b*) is similar in several ways to the 2D IR experiment, but it differs in the number of input beams and the manner by which the signal is detected. In the 2D IR experiment, three time-ordered

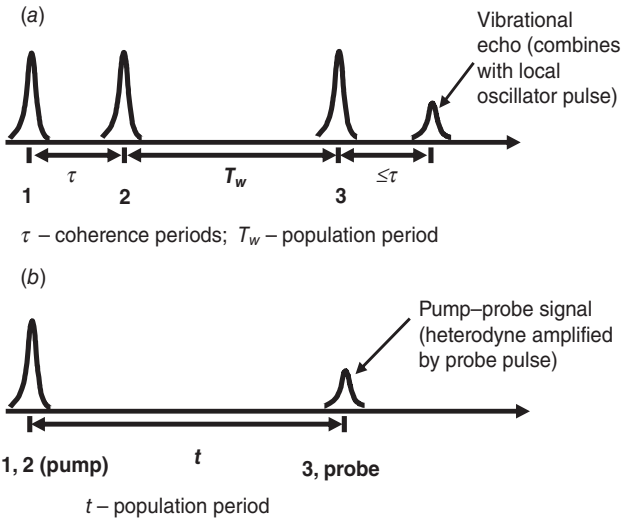

Figure 1.4 Pulse sequences implemented for (*a*) 2D IR vibrational echo spectroscopy and (*b*) pump–probe spectroscopy. Both techniques are noncollinear four-wave mixing experiments.

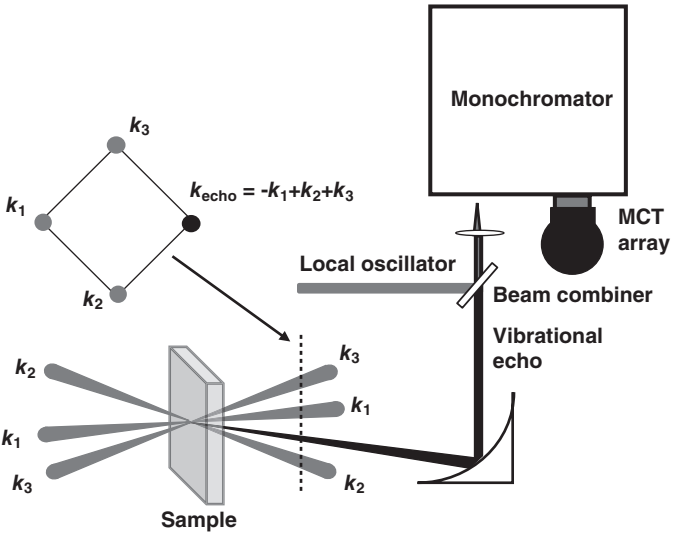

Figure 1.5 Experimental setup for the 2D IR vibrational echo experiment. Three excitation beams in a BOXCARS geometry cross in the sample to produce the vibrational echo signal in the phase-matched direction denoted by the wave vector k_{sig}. The vibrational echo signal combines with a local oscillator beam for heterodyned detection. The heterodyned signal is detected by a 32-pixel MCT array detector.

beams interact with the sample (Fig. 1.5). The first pulse induces a coherence state between the ground (0) and first excited (1) vibrational levels. The vibrations are initially in phase, but inhomogeneous broadening of the absorption line and structural fluctuations cause the phase relationships to decay. After a period of time, τ, a second pulse impinges on the sample and creates a population state in either the 0 or 1 vibrational levels. A time period T_w elapses (the waiting time) before the third pulse reaches the sample and induces a second coherence state, partially restoring the phase relationships between the vibrational chromophores. This rephasing process causes the vibrational echo signal electric field to emit at a time $t \leq \tau$. The vibrational echo signal propagates in the phase-matched direction according to $k_{sig} = -k_1 + k_2 + k_3$, as denoted by the BOXCARS geometry of the input beams shown in Figure 1.5. The vibrational echo signal is temporally and spatially overlapped with a local oscillator (LO) pulse for heterodyned detection. The LO is another IR pulse identical to the excitation pulses but lower in amplitude and fixed in time. The combined vibrational echo and LO beam is frequency dispersed by a monochromator, and the heterodyned signal is detected on a 32-pixel mercury–cadmium–telluride (MCT) array detector. If we denote the vibrational echo signal as S and LO signal as L, then the quantity $|S + L|^2 = S^2 + 2LS + L^2$ is measured on the detector. Assume S^2 is negligible and can be ignored and L^2 is a constant signal and can be subtracted. The $2LS$ cross term represents the heterodyned signal of interest.

Ultimately, the 2D IR experiment obtains frequency correlation plots (2D spectra) for the second coherence period (known as the detection time period) and

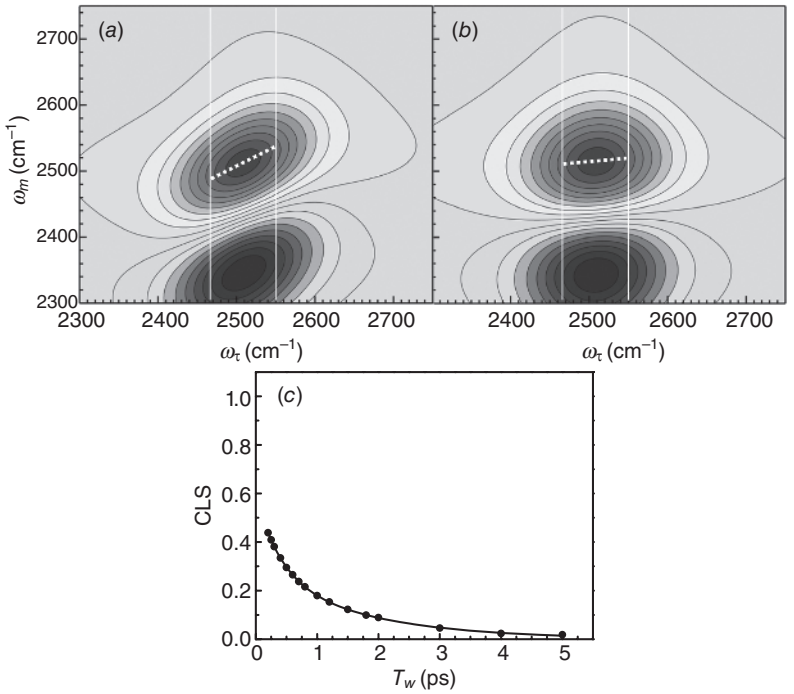

Figure 1.6 CLS procedure: (*a*) bulk water 2D spectrum at $T_w = 0.2$ ps, showing elongation along the diagonal and (*b*) bulk water spectrum at $T_w = 2$ ps. Spectral diffusion has mostly completed, so the spectra become more circular. The white solid lines show the direction of cuts during the CLS procedure. The white dots indicate the peak positions through the slices (centerline data). The slope is found through each set of peak positions at each T_w to obtain a plot of slope versus T_w, as shown in panel (*c*). The CLS curve is equal to the normalized FFCF, which is shown as the black line through the CLS data.

the first coherence period (known as the evolution time period). Each frequency axis of the correlation plot arises from Fourier transformation of each coherence period. The Fourier transform along the second coherence period is performed experimentally by the monochromator, yielding the vertical "ω_m" axis while the Fourier transform along the first coherence period is obtained numerically during data processing, yielding the horizontal "ω_τ" axis. These axes are clearly marked in Figures 1.6*a*, *b*, which show correlation spectra for bulk water (5% HOD in H_2O). During the experiment, τ is scanned for a series of fixed T_w values. As τ is scanned, the echo signal field moves in time relative to the fixed LO. The echo field goes in and out of phase with the LO field producing an interferogram. Mixing the vibrational echo signal with the LO allows interferograms to be recorded, thus providing the necessary phase information for Fourier transformation.

Qualitatively, a 2D IR vibrational echo experiment works in the following manner. The first laser pulse "labels" the initial structures of the species by establishing their initial frequencies, ω_τ. The second pulse ends the first time period τ and

starts the reaction time period T_w during which the labeled species undergo structural evolution. For example, the local hydrogen bond network rearranges. This ends the population period of length T_w and begins a third period of length $\leq\tau$, which ends with the emission of the vibrational echo pulse of frequency ω_m, which is the signal in the experiment. The vibrational echo signal reads out information about the final structures of all labeled species by their frequencies, ω_m. During the period T_w between pulses 2 and 3, the system's structural evolution occurs. The structural evolution and associated frequency changes as T_w is increased cause new off-diagonal peaks to grow in a chemical exchange experiment or the shape of the 2D spectrum to change in a spectral diffusion experiment. The growth of the off-diagonal peaks or the change in the 2D band shapes in the 2D IR spectra with increasing T_w provides the dynamical information.

The 2D IR experiments require precise timing between the excitation pulses as well as phase stability during the coherence periods. Computer-controlled precision delay lines (Aerotech ANT-50L) manipulate the delay between the excitation pulses, and a three-pulse cross-correlation measurement is used to check the timing and correct for drifts between the three excitation pulses [63]. The vibrational echo experiments are also sensitive to linear chirp in the mid-IR pulse. Linear chirp is corrected by proper insertion of materials (calcium fluoride and germanium) with opposite signs of the group velocity dispersion (GVD) [82, 83].

The 2D IR experiments presented here are used to determine the frequency–frequency correlation function (FFCF) of water molecules (OD stretch), which is a measure of spectral diffusion. The FFCF can be determined via the centerline slope (CLS) method [84, 85]. Figure 1.6 illustrates this process. In the CLS technique, the 2D IR spectrum is sliced parallel to the vertical ω_m axis over a range of frequencies surrounding the center of the 2D IR spectrum. In Figures 1.6*a*,*b*, the solid white lines show the direction of slicing and the bounds over which the slices are taken. For water systems (as shown in the figure), the range is typically $\pm$30–40 cm^{-1} around the measured center frequency of each 2D IR spectrum. Each slice intercepts a frequency on the horizontal ω_τ axis. The slices are fit to Gaussian line shape functions to determine the peak position of each slice. Only the peak positions are required. The peak positions (white dots) are plotted versus their corresponding ω_τ frequencies, and the slope of the resulting line is calculated. This process is repeated for all T_w values so that a plot of slope versus T_w is obtained (Fig. 1.6*c*). Generally, the 2D plots show elongated spectra at early T_w, as shown by Figure 1.6*a*. By 2 ps (Fig. 1.6*b*), the spectra show a more circular shape because most of the water hydroxyl environments in the H_2O inhomogeneous line shape have been sampled by the OD vibrational chromophore, indicating that spectral diffusion is nearly complete.

It has been demonstrated theoretically that the CLS curve of slope versus T_w is equal to the T_w-dependent portion of the normalized FFCF [84, 85]. The FFCF adopts a functional form that contains both homogeneous (motionally narrowed) and inhomogeneous components,

$$C_1(t) = \langle \delta\omega_{10}(t)\delta\omega_{10}(0)\rangle = \frac{\delta(t)}{T_2^*} + \sum_i \Delta_i^2 e^{-t/\tau_i} \tag{1.1}$$

where $\langle \delta\omega_{10}(t)\delta\omega_{10}(0)\rangle$ is the correlation function for the fluctuating 0–1 transition frequency, and $\delta\omega_{10}(t) = \langle\omega_{10}\rangle - \omega_{10}(t)$. The summation term in Eq. (1.1) contains the processes that sample the inhomogeneous distribution of frequencies through structural evolution of the system. The Δ_i terms are frequency fluctuation amplitudes, and the τ_i are their associated time constants. The time constants describe different time scales that contribute to spectral diffusion. The magnitude of each Δ_i term gives the contribution to the absorption line shape from processes occurring on each time scale.

The homogeneous dephasing time T_2 is given by

$$\frac{1}{T_2} = \frac{1}{T_2^*} + \frac{1}{2T_1} + \frac{1}{3\tau_{or}} \tag{1.2}$$

where T_2^* is the pure dephasing time, T_1 is the vibrational lifetime, and τ_{or} is the orientational relaxation time constant. The first term of Eq. (1.1) is known as the pure dephasing component. In the condensed phase, homogeneous broadening can arise from fast solvent motions [86]. The dynamics that give rise to pure dephasing occur on a very fast time scale such that the product $\Delta\tau < 1$, meaning that this portion of the total absorption line shape comes from a motionally narrowed (Lorentzian) component. The homogeneous component is often expressed as the homogeneous line width, $\Gamma = 1/(\pi T_2)$. In water, T_2^* is on the order of a couple hundred femtoseconds while T_1 and τ_{or} are a few picoseconds or longer. Therefore, the homogeneous line width is virtually completely determined by pure dephasing.

Figure 1.6*c* shows that there is a large difference between 1 and the initial CLS data points extrapolated to $T_w = 0$. This large drop is caused by fast homogeneous processes, and the difference between the $T_w = 0$ CLS data and 1 combined with the absorption spectrum permits the homogeneous line width to be determined. Slower processes sample the inhomogeneous distribution of frequencies and cause the T_w-dependent decay of the CLS.

The first step in extracting the FFCF involves fitting the CLS to a multiexponential decay to yield a set of amplitudes and decay constants [85]. Due to the short time approximation [85, 87, 88], the amplitude associated with the fastest of the time constants can be pushed into the homogeneous contribution. As a result, the CLS data alone cannot accurately determine the full FFCF. In order to obtain the correct homogeneous component and amplitude of the fast inhomogeneous component, it is necessary to employ the absorption line shape. The linear absorption spectrum is the Fourier transform of the linear response function, $R_1(t)$,

$$R_1(t) = |\mu_{10}|^2 e^{-i\langle\omega_{10}\rangle t} e^{-ig_1(t)} \tag{1.3}$$

where μ_{10} is the transition dipole moment of the 0–1 transition, $\langle\omega_{10}\rangle$ is the average 0–1 transition frequency, and $g_1(t)$ is the line shape function,

$$g_1(t) = \int_0^t d\tau_2 \int_0^{\tau_2} d\tau_1 \langle \delta\omega_{10}(t)\delta\omega_{10}(0)\rangle \tag{1.4}$$

Equation (1.4) contains the FFCF, as given by Eq. (1.1), showing the link between the absorption spectrum and the underlying dynamic processes. The amplitude of

Table 1.1 Bulk Water FFCF Parameters

Γ (cm^{-1})	Δ_1 (cm^{-1})	τ_1 (ps)	Δ_2 (cm^{-1})	τ_2 (ps)
76 ± 14	41 ± 8	0.4 ± 0.1	34 ± 11	1.7 ± 0.5

the fast inhomogeneous decay and the homogeneous component are the only adjustable parameters as the absorption spectrum is fit simultaneously with the CLS data. The time constants and remaining amplitudes of the CLS multiexponential fit are accurate and are fixed during the procedure. This fitting routine has been shown to accurately determine the full FFCF including both homogeneous and inhomogeneous components [84, 85]. For bulk water, it is found that there is a fast ~400-fs decay that is attributed to fluctuations of the lengths of the hydrogen bonds [89, 90], followed by a 1.7-ps decay corresponding to global hydrogen bond network randomization [23]. In addition, there is a relatively large homogeneous contribution. The full FFCF for bulk water is listed in Table 1.1 and is shown going through the CLS points in Figure 1.6*c*.

1.2.3 Polarization-Selective Pump–Probe Spectroscopy

The pump–probe experiment illustrated in Figure 1.4*b* also involves three field–matter interactions. In this variation, only two beams are used (instead of the three excitation beams plus the LO in the vibrational echo experiment). A strong pump pulse and weak probe pulse are crossed in the sample. The first two field–matter interactions occur during the pump pulse so that $\tau = 0$, and the system immediately adopts a population state in either the 0 or 1 vibrational levels. The probe pulse enters at a later time to interrogate the changes in the sample due to the pump. The pump–probe signal emits in the same phase-matched direction as the probe and self-heterodynes with the probe.

The vibrational lifetime and orientational relaxation dynamics are obtained via polarization-selective pump–probe experiments. The pump is polarized at 45° relative to the probe (which is kept at horizontal polarization). Molecules whose transition dipoles are oriented at 45° will have a higher probability of being excited, while transition dipoles oriented perpendicular to the pump will have zero probability of being excited. The probe undergoes changes in absorption due to these transitions. Because the 0–1 vibrational transition is excited, there will be increased transmission of the probe as well as stimulated emission at the 0–1 transition frequency. The induced absorption of the 1–2 transition will cause a decreased transmission of the probe at the 1–2 frequency. As the molecules reorient, fewer transition dipoles will be aligned with the pump. After the sample, the probe is resolved at parallel and perpendicular polarizations relative to the pump (±45°). The resolved probe is frequency dispersed by the monochromator and detected on the 32-pixel MCT detector. The time between the pump and probe pulses is scanned to measure the

time-dependent changes in absorption of the parallel and perpendicular components. The parallel and perpendicular signals are given by

$$I_{\parallel}(t) = P(t)(1 + 0.8C_2(t)) \tag{1.5}$$

$$I_{\perp}(t) = P(t)(1 - 0.4C_2(t)) \tag{1.6}$$

where $P(t)$ is population relaxation and $C_2(t)$ is the second Legendre polynomial orientational correlation function for a dipole transition [91]. Pure population relaxation (no contributions from orientation) may be obtained from

$$P(t) = \tfrac{1}{3}(I_{\parallel}(t) + 2I_{\perp}(t)) \tag{1.7}$$

$P(t)$ generally adopts the form of a single or biexponential decay, depending on how many distinct OD environments a system contains:

$$P(t) = e^{-t/T_1} \tag{1.8}$$

for one component or

$$P(t) = A_1 e^{-t/T_1^1} + (1 - A_1)e^{-t/T_1^2} \tag{1.9}$$

for two components, where A_1 and $1 - A_1$ are the fractional populations of components 1 and 2, respectively, and the T_1^i terms are the vibrational lifetimes of the ODs for the *i*th component. The orientational correlation function, $C_2(t)$, can be obtained from calculating the anisotropy according to

$$r(t) = \frac{I_{\parallel}(t) - I_{\perp}(t)}{I_{\parallel}(t) + 2I_{\perp}(t)} = 0.4C_2(t) \tag{1.10}$$

It is important to note that Eq. (1.10) involves dividing by the pure population relaxation [$P(t)$ of Eq. (1.7)] to obtain pure orientational relaxation dynamics. Equation (1.10) only holds for a single-component system in which the vibrational chromophores have a single vibrational lifetime and orientational correlation function. In this case, the orientational correlation function follows single exponential dynamics,

$$C_2(t) = e^{-t/\tau_{or}} \tag{1.11}$$

where τ_{or} is a time constant describing orientational relaxation. Sometimes $C_2(t)$ can also contain a contribution from a "wobbling-in-a-cone" mechanism [92, 93], which will be discussed further in Section 1.6.

If the system contains two distinct species, each with its own vibrational lifetime and orientational relaxation time constants, then $P(t)$ does not divide out and the anisotropy adopts a more complicated form [61, 68–72]:

$$r(t) = \frac{A_1 e^{-t/T_1^1} e^{-t/\tau_{or}^1} + (1 - A_1)e^{-t/T_1^2} e^{-t/\tau_{or}^2}}{A_1 e^{-t/T_1^1} + (1 - A_1)e^{-t/T_1^2}} \tag{1.12}$$

where the T_1^i and τ_{or}^i terms are the vibrational lifetimes and orientational relaxation time constants for the *i*th component, respectively. The fractional populations of each component are given as A_1 and $1 - A_1$.

1.3 LINEAR INFRARED ABSORPTION SPECTRA OF WATER NEAR CHARGED INTERFACES

1.3.1 Water in Salt Solutions

The hydroxyl stretch of water, in this case the OD stretch of HOD in H_2O, is extremely sensitive to local environments. Figure 1.7 shows the IR absorption band of the OD stretch (5% HOD in H_2O). The band is wide [~170 cm^{-1} full width at half-maximum (FWHM)] because there is a large distribution in the lengths and strengths of hydrogen bonds. Hydrogen bonds influence the attractive part of the hydroxyl vibrational potential, opening up the potential and lowering the vibrational frequency compared to the gas phase. A strong hydrogen bond will lower the vibrational transition frequency more than a weak hydrogen bond. Relative to the line center of the OD stretch of HOD in H_2O, strong hydrogen bonds produce a red shift and weak hydrogen bonds produce a blue shift [21, 23, 61, 68, 72]. Raman experiments and MC calculations have suggested that the magnitude of a red or blue shift in the hydroxyl stretch frequency is actually correlated to the strength and directionality of the electric field of the hydrogen bond acceptor [20]. Figure 1.8 shows linear IR absorption spectra of the OD hydroxyl stretch in water–salt solutions at a constant ratio of 12 water molecules to 1 salt ion pair. The OD hydroxyls will interact with the anions of the salts. The salts are KF, KCl, NaCl, KBr, NaBr, KI, and NaI. As the size of the anion increases, the spectra show a greater blue shift. This trend has been observed by other groups [21, 94]. Based on the Raman and MC studies mentioned above, the blue shift arises because a more diffuse and less directed electric field is projected along the OD hydroxyl as the size of the anion increases. KF, in contrast, causes the spectrum to red shift compared to the OD stretch of HOD in bulk water. F^- is a very small anion, increasing the electric field felt by the hydroxyl. The Raman and MC study also concluded that the anion only caused local changes to the hydrogen bond structure of water and that only the waters in the first solvation

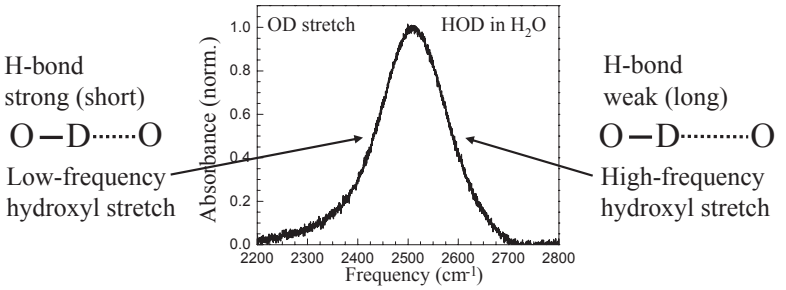

Figure 1.7 Linear IR absorption spectrum of the OD stretch of 5% HOD in H_2O. The absorption band is very wide (~170 cm^{-1}) because there is a wide range in the distribution of lengths and strengths of hydrogen bonds in the water network. The red side of the line shape is dominated by strong hydrogen bonds that lengthen the OD bond. In contrast, the blue side of the line is dominated by weak hydrogen bonds that cause a shorter OD bond length.

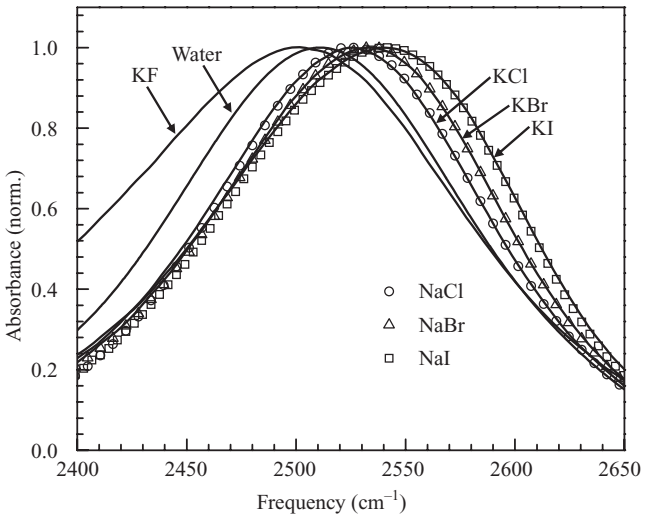

Figure 1.8 Linear IR absorption spectra of bulk water (5% HOD in H_2O) and water–salt solutions at ratios of 12 : 1 water to salt. The salts are KF, KCl, KBr, KI, NaCl, NaBr, and NaI. As the anion increases in size, the spectra shift more to the blue. Large anions exert a weaker electric field along the OD hydroxyl to cause the blue shift. There appears to be no difference when the cation is changed but the anion kept the same.

shell of the anion felt significant perturbation [20]. The amount of blue or red shift is correlated to electric field strength of the anion and also may reflect the strength of the hydrogen bond. These conclusions refute the idea that salts are either kosmotropes ("structure makers") or chaotropes ("structure breakers") [95] since any changes in hydrogen bonding structure are very localized. It can also be seen from Figure 1.8 that changing the identity of the cation (K^+ to Na^+) does not affect the spectra when the anions are kept the same. The lack of change with cation identity indicates that it is the direct very local interaction of the hydroxyls and anions that determines the hydroxyl stretch frequency.

The spectra in Figure 1.8 only show one broad absorption band even though there are arguably two types of water molecules in each system: water hydrogen bonded to other water hydroxyls and water interacting with ions. The water–$NaBF_4$ system, in contrast, shows different behavior. Linear IR absorption spectra of the 1.7-M, 3.1-M, 4.3-M, and 5.5-M solutions are shown in Figure 1.9 [25]. Bulk water shows a single absorption band at ~2509 cm^{-1}, but at 1.7 M $NaBF_4$ concentration and higher concentrations, a second, narrower band grows in at ~2650 cm^{-1}. Because this second band increases in size as the $NaBF_4$ concentration increases, it is concluded that this second band is due to water hydroxyls interacting with the tetrafluoroborate anions. The main band at ~2509 cm^{-1} in the spectra is attributed to water–water interactions. As discussed below, in this system, 2D IR chemical exchange spectroscopy can be used to directly measure the exchange rate between the water–ion and water–water species because cross peaks will be resolved.

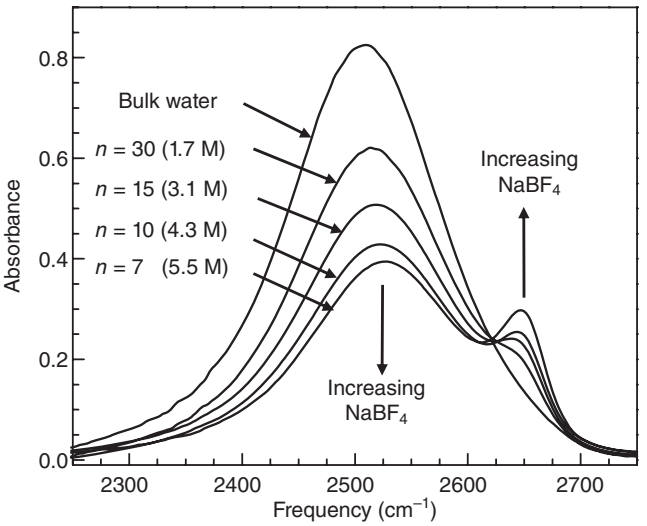

Figure 1.9 Linear IR absorption spectra for water–$NaBF_4$ solutions at varying concentrations. The main lobe around 2509 cm^{-1} corresponds to water–water hydrogen bonding environments while the smaller peak around 2650 cm^{-1} corresponds to water molecules interacting with the tetrafluoroborate anions. As the $NaBF_4$ concentration increases, the main lobe decreases in size, and the smaller lobe increases.

1.3.2 Water in AOT Reverse Micelles

Figure 1.10 displays linear IR absorption spectra for water (5% HOD in H_2O) inside the full range of reverse micelle w_0's examined, from $w_0 = 2$ to $w_0 = 46$. For clarity, a few w_0's are omitted because they closely overlap with neighboring spectra. As the reverse micelle size decreases, the spectra systematically shift to the blue. While bulk water peaks around 2509 cm^{-1}, the $w_0 = 2$ spectrum peaks around 2565 cm^{-1}. This blue shift trend occurs because as reverse micelle size decreases, proportionally more water molecules interact with the sulfonate head groups [61, 68, 70]. The sulfonate group is a large anion, so it exerts a weak electric field along the OD hydroxyl stretch.

Figure 1.1 illustrates that distinct water environments exist in the reverse micelle. If large enough, the reverse micelle can support a core of bulklike water. The bulk water core is then surrounded by a layer of interfacial water molecules associated with the head group interface. It has been shown that the spectra in Figure 1.10 can be reproduced by a linear combination of the spectrum of bulk water and the spectrum of $w_0 = 2$ [61, 68, 70]. In the $w_0 = 2$ sample, essentially all of the water molecules interact with the head groups, and there is no bulklike core. The $w_0 = 2$ spectrum is taken to be the spectrum of interfacial water. This model of decomposing the reverse micelle spectra into bulk and interfacial contributions has been referred to as the core–shell model and is described by

$$I_{\text{tot}}(\omega) = a_1 I_1(\omega) + (1 - a_1) I_2(\omega) = S_1(\omega) + S_2(\omega) \tag{1.13}$$

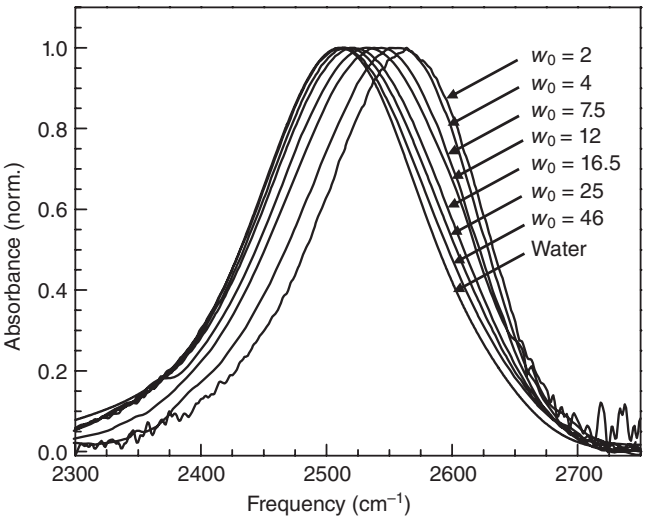

Figure 1.10 Linear IR absorption spectra for water inside AOT reverse micelles from $w_0 = 2$ through $w_0 = 46$ along with bulk water for comparison. The spectra steadily shift to the blue as the reverse micelle size decreases.

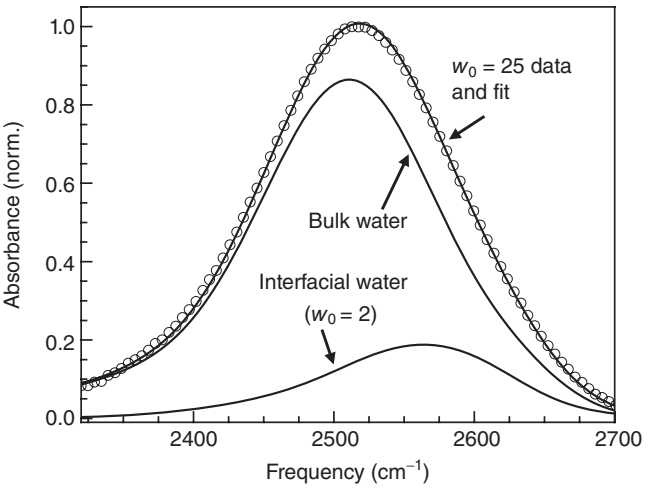

Figure 1.11 Two-component decomposition of the water spectrum of AOT $w_0 = 25$, a large reverse micelle. The $w_0 = 25$ spectrum can be reproduced by a linear combination of the bulk water spectrum and the $w_0 = 2$ spectrum in which nearly all the water molecules interact with the head group interface.

where I_1 and I_2 are the component spectra for bulk water and $w_0 = 2$, respectively, and a_1 is the fractional population. When fitting the reverse micelle spectra, a_1 is the only adjustable parameter. Figure 1.11 displays the core–shell decomposition for AOT $w_0 = 25$. The circles are the data and the solid line through the circles is the weighted sum of the bulk water spectrum and the $w_0 = 2$ spectrum. The agreement

Table 1.2 Fractional Population of Interfacial Water in Large AOT Reverse Micelles

w_0	Diameter (nm)	IR Fraction	Geometric Fraction
25	9	0.17	0.18
37	17	0.10	0.10
46	20	0.08	0.08

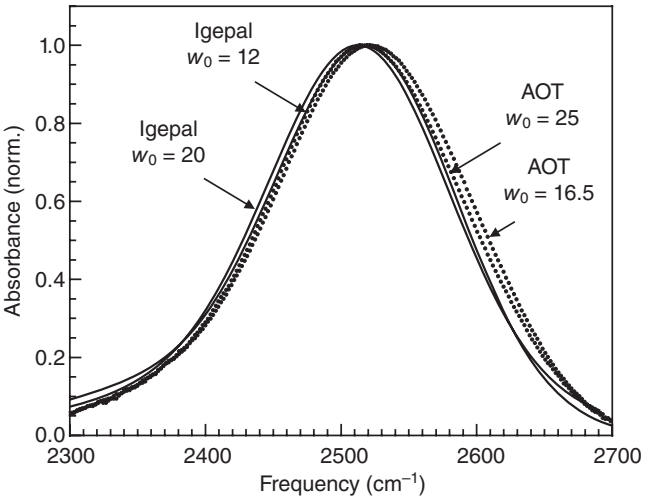

Figure 1.12 Linear IR absorption spectra for water inside Igepal reverse micelles compared to AOT reverse micelles of the same size. Igepal $w_0 = 20$ has the same size as AOT $w_0 = 25$ (9 nm diameter), and Igepal $w_0 = 12$ has the same size as AOT $w_0 = 16.5$ (5.8 nm). Spectra for systems of the same diameter are not equivalent to each other, indicating that the hydrogen bonding interactions in the Igepal and AOT systems are different.

between the original spectrum and the linear combination is excellent. Table 1.2 [70] lists the $1 - a_1$ parameter (interfacial fraction) for AOT reverse micelles of $w_0 = 25$, 37, and 46. The numbers indicate that the fraction of interfacial water decreases as water pool diameter increases. Fractions are listed for both the IR spectral decomposition analysis as well as geometric calculations. If the interfacial region is modeled as a shell of approximately one water molecule thick (about 2.8 Å), then the interfacial fractions are nearly identical to those obtained by spectral analysis. These results strongly indicate that in large reverse micelles, the interface gives rise to a very locally perturbed region of interfacial water that does not extend far beyond the first solvation shell of the head groups [70].

1.3.3 Water in Igepal Reverse Micelles

The linear IR absorption spectra of water inside of Igepal reverse micelles, as shown in Figure 1.12, also show a systematic blue shift as the water pool diameter decreases [71].

Figure 1.12 compares spectra of water in Igepal reverse micelles to water in AOT reverse micelles of the same size. Igepal $w_0 = 20$ and AOT $w_0 = 25$ each have a water pool diameter of 9 nm while Igepal $w_0 = 12$ and AOT $w_0 = 16.5$ each have a water pool diameter of 5.8 nm. The Igepal spectrum of a given w_0 is not as blue shifted as its AOT counterpart of the same size even though both systems contain identical amounts of water. It is important to note that identical w_0's of Igepal and AOT do not yield the same water pool diameters because of different aggregation numbers of the two surfactants; that is why different w_0's are used to produce reverse micelles of the same size. Igepal reverse micelles, like the AOT systems, also contain bulk and interfacial water regions. In the case of Igepal, the waters interact with hydroxyl head groups, but in AOT they interact with charged sulfonate head groups. The chemical identity of the interface clearly alters the linear absorption behavior of the water molecules.

The Igepal spectra are not decomposed into core and shell regions like the AOT systems because Igepal reverse micelles are not well characterized below $w_0 \sim 10$ [78], so there is no low water content spectrum (akin to AOT $w_0 = 2$) to approximate the pure interfacial water spectrum. Furthermore, the Igepal reverse micelle system contains a third environment in addition to the core and interfacial water regions. The hydroxyl head groups will exchange deuterium atoms with the 5% HOD in the water pool. As a result, the interfacial region is composed of two types of hydroxyls: waters at the interface and OD head groups. The population of OD head groups is small, and their contribution to the experimental observables has been treated in detail so that the interfacial water dynamics can still be extracted (see Section 1.4.2) [71]. Figure 1.12 shows that there are significant spectral changes upon changing the chemical identity of the interface, but it will be shown below that changing the charged sulfonate head groups at the interface to neutral hydroxyl groups does not significantly affect water's hydrogen bonding dynamics.

1.4 POPULATION RELAXATION AND ORIENTATIONAL RELAXATION

1.4.1 At the Interface of Large and Intermediate AOT Reverse Micelles

The spectral analysis in Section 1.3.2 shows that large reverse micelles can be divided into two distinct regions: bulklike core water and interfacial water. This core–shell model (Fig. 1.11) has critical implications in the treatment of large reverse micelles, as it implies that the dynamics of the core and interface regions can be separated as well, with the core exhibiting the dynamics of pure water. In pure water, the vibrational lifetime of the OD stretch is 1.8 ps [using Eq. (1.8)] [68, 70], and the orientational relaxation time is 2.6 ps [using Eq. (1.11)] [96]. Consequently, the interfacial dynamics are the only unknowns in measurements on the water pools of large reverse micelles. Based on spectral analysis, waters that interact with the interface experience a blue shift in their linear IR absorption spectra. As shown by

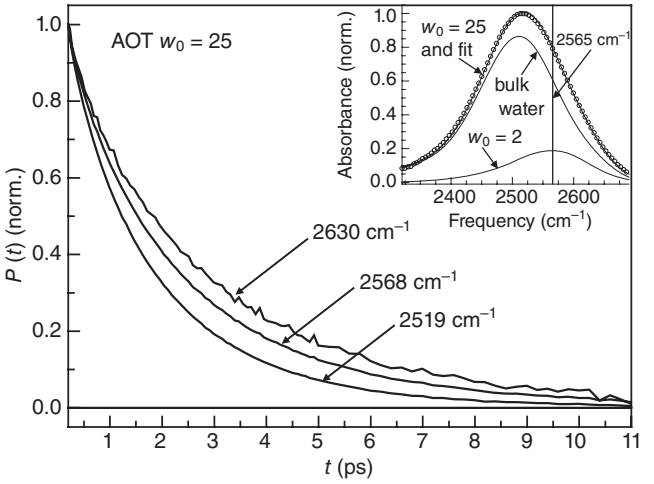

Figure 1.13 Population relaxation data for AOT $w_0 = 25$ at three detection frequencies. The inset shows that interfacial water molecules have more population at frequencies above 2565 cm^{-1}. The three curves have a slight frequency dependence to them because of changing fractions of core and interfacial water.

the inset in Figure 1.13, the nearly purely interfacial $w_0 = 2$ OD–water spectrum peaks at 2565 cm^{-1}. The experimental pump-probe signal is frequency dispersed by a monochromator, so the dynamics at different frequencies across the absorption line shape can be monitored. For example, if the dynamics of $w_0 = 25$ were measured at 2519 cm^{-1}, then water molecules sampling the center of the absorption line shape would be mostly observed. Most of the spectral contribution at that frequency is due to bulklike water molecules in the core, as shown by Figure 1.11 and the inset in Figure 1.13. At higher frequencies, such as 2565 cm^{-1}, the water molecules at the surfactant interface make a larger contribution to the signal than they do toward the center of the absorption line. To accurately extract the dynamics at the interface from the dynamics of the core (which are known), it is useful to have the greatest amount of interfacial water contributing to the signal as possible. Because of this requirement, it is best to analyze the pump–probe signals detected at frequencies greater than or equal to 2565 cm^{-1} where it is likely that a significant portion of the signal comes from interfacial water.

Figure 1.13 displays the population relaxation decay curves [Eq. (1.7)] for $w_0 = 25$ at three different frequencies: 2519 cm^{-1} (near the absorption center of $w_0 = 25$), 2568 cm^{-1} (near the peak absorption of $w_0 = 2$ interfacial water), and 2630 cm^{-1} (far to the blue) [70]. The three curves are not the same, indicating that there is a frequency dependence to the population decay. When there are two separate water ensembles, the population decay is the weighted sum of the population decay of the two components, as given by Eq. (1.9). When the curves in Figure 1.13 are fit to Eq. (1.9), the vibrational lifetime of the first component (bulk water) is kept constant at its literature value such that $T_1^{\mathrm{w}} = 1.8$ ps at all frequencies. The super-

Table 1.3 Interfacial Vibrational Lifetime, T_1^{int}, and Orientation Relaxation Times, τ_{or}^{int}, for Large AOT Reverse Micelles

w_0	12	16.5	25	37	46
T_1^{int} (ps)	4.7 ± 0.2	4.4 ± 0.3	4.3 ± 0.5	4.6 ± 0.5	3.9 ± 0.5
τ_{or}^{int} (ps)	23 ± 2	17 ± 3	19 ± 3	18 ± 3	18 ± 3

script *w* stands for the lifetime of the OD stretch of dilute HOD in bulk water. Data at all three frequencies are fit simultaneously to Eq. (1.9), and A_1 (the fractional population) and T_1^{int} (the interfacial water lifetime) are the only adjustable parameters. It is found that this two component model for the population decay accurately describes the population relaxation dynamics for all AOT reverse micelles of $w_0 = 12$ and larger. For all reverse micelles of $w_0 \geq 12$, the vibrational lifetime of interfacial water molecules is found to be 4.3 ± 0.5 ps. This value of ~4.3 ps remains constant regardless of w_0 and regardless of frequency, indicating that the dynamics of water at the interface are quite distinct from those of the bulk water core in large reverse micelles [68, 70]. Table 1.3 lists the obtained T_1^{int} values for the large reverse micelles, showing the invariability. The only parameter that changes with wavelength (leading to the three different curves in Figure 1.13) is A_1. As frequency increases, the amount of interfacial water increases, so $1 - A_1$ becomes larger. As w_0 decreases, there is more interfacial water overall, so the $1 - A_1$ values collectively increase.

Because there are two components to the population relaxation, the orientational relaxation must also be fit to a two-component model, as described by Eq. (1.12). There are quite a few variables in this equation, but population relaxation analysis allows many of the parameters in Eq. (1.12) to be fixed. A_1, T_1^w, T_1^{int}, and τ_{or}^w (the known bulk water reorientation time of 2.6 ps) all can be fixed, leaving the orientational relaxation time of the interface, τ_{or}^{int}, as the only adjustable parameter. Figure 1.14 shows the anisotropy decays [Eq. (1.10)], for several detection wavelengths for the $w_0 = 25$ reverse micelle [70]. The plateaus in the data sets, which become apparent around 5 ps, are characteristic of two-component systems [70, 72]. The sensitivity of the shape of the anisotropy curves to the interfacial orientational relaxation time is shown in Figure 1.15. All of the parameters are held constant in these model calculations except for τ_{or}^{int}. The dotted line in Figure 1.15 indicates the end of the experimentally accessible data acquisition time window. At long time all of the curves decay to zero, but the strength of the signal is limited by the vibrational lifetimes of the OD chromophores, and therefore the signal dies out before the experimental anisotropy data decays to zero.

The experimental anisotropy data at several wavelengths, like those shown in Figure 1.14, for each w_0 were fit simultaneously to Eq. (1.12) to determine the value for τ_{or}^{int}. As shown in Table 1.3 $\tau_{or}^{int} = 18 \pm 3$ ps is obtained for w_0 values of 12–46. This value of 18 ps remains constant regardless of the w_0 or the frequency observed for these large reverse micelles. The only parameter that changes, as dictated by the population relaxation analysis, is the fractional population, A_1.

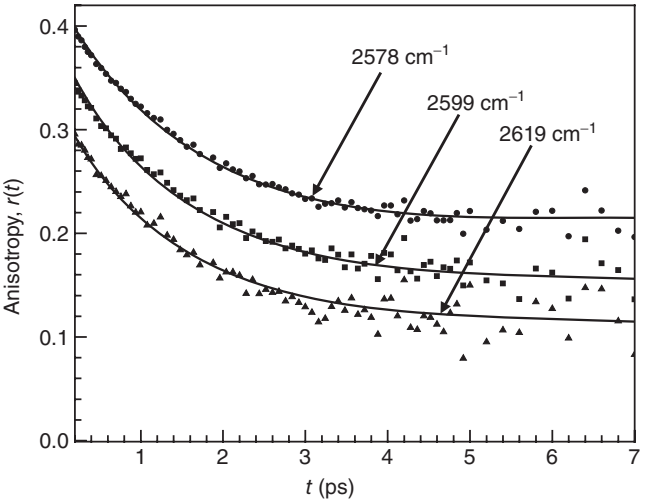

Figure 1.14 Anisotropy curves for AOT $w_0 = 25$ at three detection frequencies. The data show plateaus around 5 ps that are characteristic of two-component systems. The curves are offset by ~0.05 for clarity. The solid lines are fits to the data using the two-component anisotropy model.

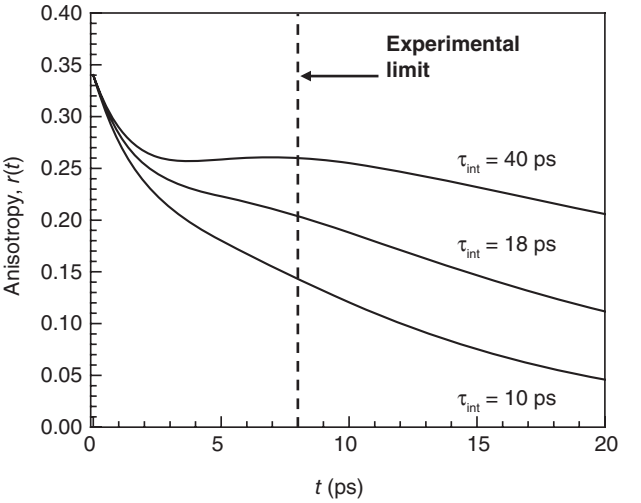

Figure 1.15 Calculated anisotropy decays of a two-component system. The different curves are produced by using different values for the interfacial orientational relaxation time constant while keeping all other parameters in the two-component anisotropy equation constant. At long time, all of the curves decay to zero. The dashed line shows the maximum time for experimental data collection. When the anisotropy data are analyzed to this point, it appears as if there is a plateau that would normally correspond to a component that undergoes infinitely slow rotation.

Table 1.4 Core and Interfacial Vibrational Lifetimes and Orientation Relaxation Times for Intermediate AOT Reverse Micelles

w_0	7.5	10
T_1^{w} (ps)	2.1 ± 0.2	2.2 ± 0.3
T_1^{int} (ps)	5.5 ± 0.2	5.3 ± 0.3
τ_{or}^{w} (ps)	4.4 ± 0.2	4.0 ± 0.3
τ_{or}^{int} (ps)	30 ± 5	26 ± 3

Intermediate-sized reverse micelles, such as $w_0 = 10$ and $w_0 = 7.5$ also show two-component vibrational lifetime behavior that separates into core and interfacial contributions, but the core does not follow bulk water dynamics. The dynamics in both regions increase in value from their counterparts in the large reverse micelles. The core has a vibrational lifetime of ~2 ps, and the interfacial waters have a vibrational lifetime of ~5.3 ps (Table 1.4) [63, 68]. Because the core does not follow bulk dynamics, the orientational lifetimes of both the core waters and interfacial waters, τ_{or}^{w} and τ_{or}^{int} in Eq. (1.12), respectively, are unknown. Simultaneous fitting at several frequencies for each w_0 yield a core orientational lifetime of ~4 ps and an interfacial orientational lifetime of ~30 ps. These results indicate that the effects of confinement become more pronounced in smaller sizes. Again, the important observation is that the population and orientational lifetimes for the core and interface of intermediate reverse micelles do not change with w_0 or frequency and that only the fractional populations change.

The $w_0 = 10$ AOT reverse micelle has a water pool with a diameter of 4 nm. The fact that the core water no longer has bulk water properties sets a distance scale for the influence of the interface on water molecules away from the interface. As discussed above, the interface has a very substantial influence on water in the first water layer adjacent to the interface. Water molecules beyond the first layer are also perturbed. In the spherical reverse micelles, the influence of the interface is propagating in all directions. The fact that the core of the $w_0 = 10$ water pool is affected indicates that as the reverse micelles become smaller and the radius of curvature of the interface becomes smaller, the influence of the interface propagates out ~2 nm.

1.4.2 Neutral versus Ionic Interfaces

The AOT head group interface contains both negatively charged sulfonate head groups and positively charged sodium counterions. It is reasonable to consider how much the presence of these charged moieties affects the interfacial water dynamics. To determine the role of interfacial charges, orientational dynamics were measured for water inside of Igepal reverse micelles. Igepal (Fig. 1.2) is terminated with neutral hydroxyl head groups. Water dynamics in Igepal $w_0 = 12$ and $w_0 = 20$ were

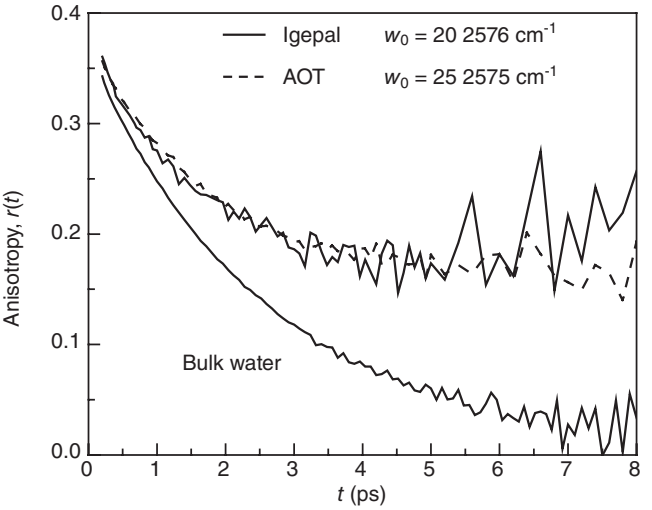

Figure 1.16 Anisotropy data for Igepal $w_0 = 20$ and AOT $w_0 = 25$ compared to bulk water. The data for the reverse micelles are nearly identical, showing that the chemical identity and charged nature of the interface have only minor effects on water dynamics. The presence of the interface is the dominant factor.

examined. These systems have the same water pool diameters as AOT $w_0 = 16.5$ (5.8 nm) and $w_0 = 25$ (9 nm), respectively. The linear IR absorption spectra in Figure 1.12 shows that the nature of the hydrogen bonding interactions are different in the two reverse micelles, as seen by the small, but clear, red shift of the Igepal spectra from their AOT counterparts of the same size.

Anisotropy data at a detection frequency of ~2575 cm^{-1} for Igepal $w_0 = 20$ and AOT $w_0 = 25$ are shown in Figure 1.16. The two curves are nearly identical, although the Igepal turns slightly up at long time, and there is also some difference at early time. Because Igepal contains hydroxyl groups that exchange with the deuterium of the HOD molecules, the Igepal data must be fit with a modified three-component model for the anisotropy and population relaxation [71]. When the data are fit in this way, the water reorientation times for Igepal $w_0 = 12$ and $w_0 = 20$ at the interface are the same within experimental error: 15 ± 3 ps and 13 ± 4 ps, respectively [71]. The reorientation time of the hydroxyls are assumed to be infinitely long (coupled to the rotation of the whole micelles), and the core adopts the bulk water reorientation time (2.6 ps). Note that the reorientation time for waters at the AOT interface are 18 ± 3 ps. The error bars of the Igepal and AOT results overlap to some extent. Therefore, the interfacial orientational relaxation in Igepal is either the same or at most slightly faster than in AOT. The orientational relaxation is directly related to the hydrogen bond dynamics. The important point of these results is that going from a charged interface to a neutral one at most makes a modest difference in the dynamics. The presence of the interface has the largest impact on the dynamics, while the chemical nature of the interface, including its charged moieties, has less of an effect.

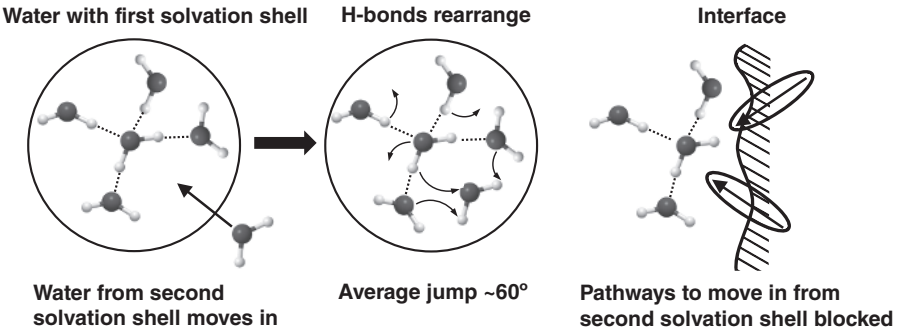

Figure 1.17 Illustration of hydrogen bond network reorientation and reorganization through jump reorientation. The mechanism involves concerted motions of the first and second solvation shells of water molecules. The presence of an interface physically eliminates pathways by which jump reorientation can occur, regardless of its chemical composition.

Figure 1.17 illustrates schematically how water undergoes orientational relaxation in bulk water and the role that an interface plays in slowing down reorientation. Figure 1.17 is a very qualitative illustration in two dimensions of what are really three-dimensional structures and processes. In bulk water, orientational relaxation involves concerted hydrogen bond rearrangement that results in jump reorientation [66, 67]. In the left portion of the figure, a central water molecule makes four hydrogen bonds to other water molecules in its first solvation shell. A fifth water moves in from the second solvation shell. Because the water hydrogen bonding network is continually in motion, it may become favorable for the water molecule to form a hydrogen bond with the fifth water that has come into its solvation shell. After going through a five-coordinate transition state involving a bifurcated hydrogen bond with two water molecules, the central water can make a large angular jump of ~60° to switch hydrogen bonds with that fifth water molecule [66, 67]. The surrounding water molecules move and reorient concertedly to accommodate these motions such that nonhydrogen-bonded hydroxyls do not exist for any significant length of time. The right-hand portion of the figure suggests the role that an interface or large molecule, such as a protein, plays. The interface blocks many of the pathways for water to move into the first solvation shell, which greatly reduces the number of pathways that can give rise to jump reorientation. The interface eliminates an entire half-space of water molecules. In addition, the rough surface topography of the interface also inhibits water molecules from moving into the first solvation shell along a range of paths that are approximately parallel to the interface. Thus the presence of the interface or other physical hindrance, such a large molecule, reduces the rate of jump reorientation independent of the chemical nature of the blocking species.

1.4.3 The Role of Interfacial Geometry

In the previous sections it was shown that the presence of an interface is enough to significantly impact water orientational relaxation and hydrogen bond dynamics. The

chemical composition of the interface for charged versus neutral but polar hydrogen bonding interfaces has a relatively minor impact on the dynamics. In this section, water dynamics in two different confinement geometries are compared, that is, water in AOT reverse micelles and AOT lamellar structures (2D slabs of water). Water dynamics are compared for samples of the same hydration level (w_0 and λ) and also samples that have the same nanoscopic dimension. The nanoscopic dimension is the surface-to-surface distance in the two types of structures: the diameter for the reverse micelles and distance between the interfacial planes for lamellar structures. The w_0 parameter for lamellar structures is denoted as λ. As an example, $\lambda = 46$ and $w_0 = 46$ have the same amount of water per AOT molecule, but the $w_0 = 10$ reverse micelle has the same nanoscopic dimension as $\lambda = 46$. Both distances are 4.0 nm. In all of the lamellar samples, the separation between the planar interfaces is sufficiently large that the center of the 2D water slab has bulklike water dynamics. This is true even though the separation of the planes, for example, 4 nm for $\lambda = 46$, can be in the range where for the same diameter reverse micelles, the core would not be bulk water. The difference arises because the planar slabs of water are infinite in two directions and only confined in one direction. In contrast the spherical water nanopools of reverse micelles are confined in all directions.

Figure 1.18 [69] shows the anisotropy curves for four sets of reverse micelle/lamellar systems. In all cases, the samples with the same hydration level are almost

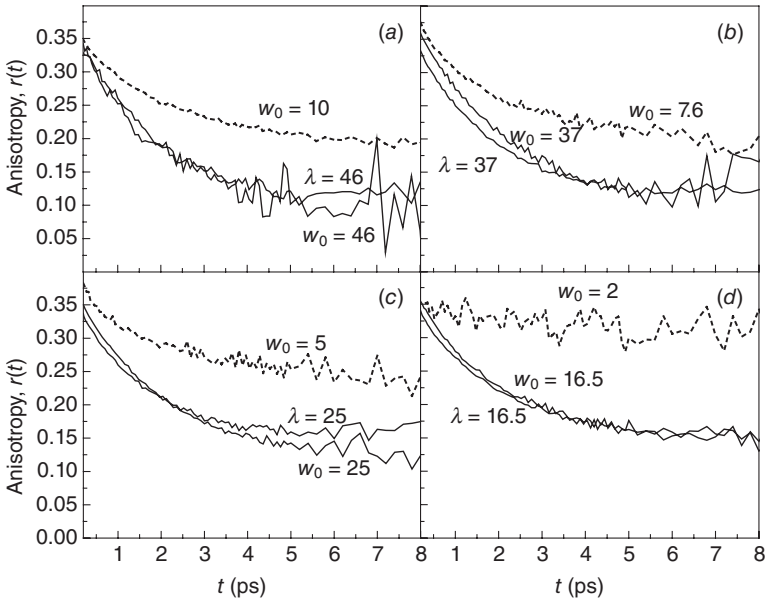

Figure 1.18 Anisotropy data comparing water dynamics for reverse micelles (w_0) and lamellar structures (λ) of the same hydration level and surface-to-surface distance. Samples with the same hydration level (e.g., $w_0 = 46$ and $\lambda = 46$) have more similar dynamics than for samples with the same surface-to-surface distance (e.g., $w_0 = 10$ and $\lambda = 46$).

the same, while the samples with the same nanoscopic dimension (surface-to-surface distance) are very different. Analysis of the data shows that the vibrational lifetimes and reorientation times of water at the lamellar interfaces are the same as those in the large reverse micelles; 4.3 ps for vibrational lifetimes and 18 ps for orientational relaxation times [69]. The anisotropy decay curves for the lamellar structures are not identical to their reverse micelle counterparts of the same hydration level. This occurs because the flat geometry of the lamellar structures results in greater surface area per AOT head group. In reverse micelles, the surface area varies from <30 $Å^2$ in $w_0 = 2$ to a limiting value of 54 $Å^2$ in $w_0 = 40$ and higher [60]. In the lamellar structures, the surface area per AOT molecule is 65 $Å^2$ [97]. Therefore, there is a higher population of interfacial water in the lamellar structures for a given hydration level.

Overall, these results indicate that an interface only gives rise to a substantial perturbation of the water dynamics over a short range, approximately one solvation shell of waters at the interface. The hydration level of the reverse micelles and the lamellar structures mainly determines the dynamics. The surface-to-surface distances of the systems have little to no effect. For instance, in Figure 1.18*d*, the $\lambda = 16.5$ lamellar structure has a surface-to-surface distance of 1.7 nm (the same distance as the diameter of $w_0 = 2$), but the dynamics are almost the same as $w_0 = 16.5$ reverse micelles with a diameter of 5.8 nm. In addition, the values for interfacial water vibrational lifetime and reorientation in the lamellar structures were the same within experimental error as those for interfacial water in AOT reverse micelles (4.3 and 18 ps, respectively), indicating that the dynamics are mainly determined by the presence of an interface and how many waters interact with it.

1.5 ION–WATER HYDROGEN BOND SWITCHING

Two-dimensional IR chemical exchange experiments were conducted on concentrated solutions of sodium tetrafluoroborate ($NaBF_4$) [25]. Figure 1.19 shows a schematic illustration of spectra for an ideal 2D IR chemical exchange experiment. There are two species, A and B, with absorption frequencies, ω_A and ω_B. At short time (top panel), prior to any chemical exchange, there are two peaks on the diagonal that arise from the 0–1 vibrational transition (black, positive going), and there are two corresponding peaks below them that occur from vibrational echo emission at the 1–2 transition frequency (gray, negative going). The 1–2 peaks are shifted to lower frequency along the ω_m axis by the amount of the vibrational anharmonicity. At long time (bottom panel), chemical exchange has occurred. Some A's have turned into B's, and the same number of B's have turned into A's. Because the system is in equilibrium, the number of A's turning into B's equals the number of B's turning into A's per unit time. In other words, the rate of A's going to B's equals the rate of B's going to A's. Chemical exchange is manifested by the growth of the off-diagonal peaks. Measurement of the time-dependent increase in the off-diagonal peaks, accounting for the vibrational lifetime and orientational relaxation that cause all peaks to decrease in amplitude, gives the time dependence of the chemical exchange

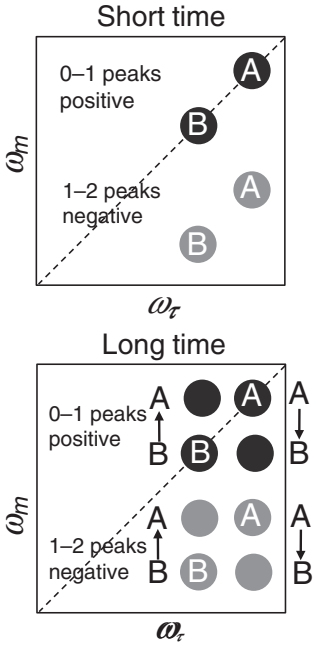

Figure 1.19 Ideal chemical exchange system. The black diagonal peaks correspond to the 0–1 vibrational transition while the gray peaks correspond to the 1–2 vibrational emission and appear off-diagonal due to the vibrational anharmonicity. At short time, only diagonal peaks (and their 1–2 off-diagonal peaks) appear. At long time, chemical exchange causes cross peaks to grow in.

[55]. Vibrational excitation of the OD stretch does not change the equilibrium or the rates of chemical exchange processes [55].

In the schematic shown in Figure 1.19, the anharmonicity is large enough that the positive 0–1 peaks do not overlap with the negative 1–2 peaks. However, for the $NaBF_4$–water chemical exchange experiments, the anharmonicity of the OD hydroxyl bound to an anion (ha, hydroxyl/anion) is much smaller than the anharmonicity of the hydroxyl bound to a water oxygen (hw, hydroxyl/water). Therefore, positive- and negative-going peaks overlap as the off-diagonal chemical exchange peaks grow in. Figure 1.20*a* shows the 2D IR spectrum of water in a 5.5-M $NaBF_4$ solution at short time ($T_w = 0.2$ ps). At this short time, no chemical exchange has occurred. The peaks on the diagonal are the 0–1 positive-going ha and hw peaks. The negative-going 1–2 ha peak is below the diagonal ha peak. The negative-going 1–2 hw peak is not shown. In Figure 1.20*b* the spectrum is shown at 4 ps. Chemical exchange has produced large changes in the spectrum. The off-diagonal positive exchange peak to the left of the ha peak and above the hw peak can be clearly seen. The corresponding positive exchange peak that would be below the ha peak and to the right of the hw peak is on top of the negative-going 1–2 ha peak. In addition, one of the negative-going 1–2 exchange peaks appears right in the middle of the positive-going diagonal 0–1 hw peaks. It is manifested by essentially negating the center of the diagonal 0–1 hw peak. In spite of the overlapping peaks, the chemical exchange data can be readily analyzed because the frequencies at which all of the peaks will appear are precisely known [25].

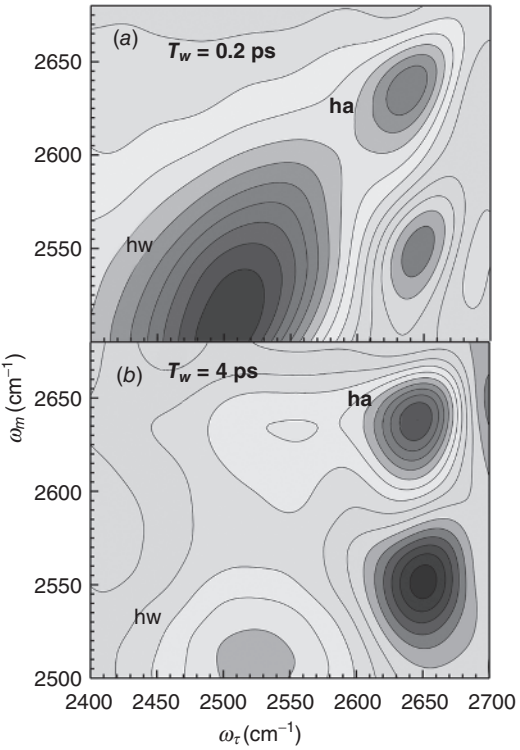

Figure 1.20 Two-dimensional correlation plots for the 5.5-M $NaBF_4$ solution showing chemical exchange. At early T_w only the peaks due to hydroxyl–water interactions (hw) and hydroxyl–anion interactions (ha) are observed. At later T_w chemical exchange has occurred as seen by the growth of off-diagonal cross peaks.

To extract the exchange time in the $NaBF_4$ system, the peak volumes of the diagonal and off-diagonal peaks are measured. The peak volumes reflect the various populations. Figure 1.21 shows the results of the peak-volume analysis of the 2D IR spectra taken over a range of T_w's. The diagonal peaks in Figure 1.21 decay because of chemical exchange, population relaxation, and orientational relaxation. The off-diagonal peaks grow in because of chemical exchange but decay because of the other processes. The solid curves through the data in Figure 1.21 are the result of a single adjustable parameter fit that yields the chemical exchange time. Because the system is in equilibrium, the dynamics can be characterized by a single time constant (the inverse of the rate constant for water bound to an anion going to water bound to another water). The analysis yields the time for a water molecule hydrogen bonded to a BF_4^- anion to switch to being bonded to an oxygen of another water molecule. The exchange time is determined to be 7 ps [25]. This should be compared to the hydrogen bond exchange time in pure water of ~2 ps obtained from 2D IR measurements of spectral diffusion [38, 39]. The important point is that ions slow the rearrangement of hydrogen bonds, but only by a factor of 3 or 4. The relatively mild affect of ions on hydrogen bond switching may account for the relatively small difference between the interfacial dynamics of water in contact with charged versus neutral interfaces, as seen by the comparison of water dynamics in AOT and Igepal reverse micelles in Section 1.4.2.

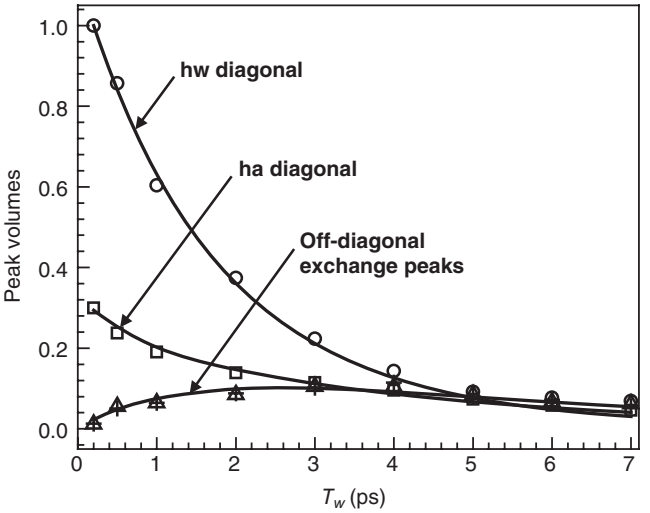

Figure 1.21 Peak-volume data used to obtain the 7-ps exchange time for water hydrogen bonded to an anion to switch to being hydrogen bonded to a water hydroxyl.

Table 1.5 Population Relaxation Parameters for Small AOT Reverse Micelles[a]

Sample	Parameter	2590 cm^{-1}	2610 cm^{-1}	2620 cm^{-1}	2640 cm^{-1}
AOT $w_0 = 2$	A_1	0.13	0.08	0	0
	T_1^1 (ps)	2.0	2.0	–	–
	T_1^2 (ps)	7.3	7.5	7.4	8.1
AOT $w_0 = 4$	A_1	0.22	0.15	0.13	0.10
	T_1^1 (ps)	2.0	2.0	2.0	2.0
	T_1^2 (ps)	6.4	6.6	6.9	7.4

[a]Error bars are ±0.2 ps for time constants, ±0.04 for amplitudes; $A_2 = 1 - A_1$.

1.6 SMALL REVERSE MICELLES

The small reverse micelles of $w_0 = 2$ and $w_0 = 4$ have diameters of 1.7 and 2.3 nm, respectively, and cannot support a distinct core region. Surprisingly, these reverse micelles present a situation where, even though the water molecules exist in a mainly interfacial environment without a core region, population relaxation still has two components, as shown by Table 1.5 [63]. For both $w_0 = 2$ and $w_0 = 4$, there is one lifetime of 2 ps and a slower lifetime of ~7 ps for $w_0 = 2$ and ~6.5 ps for $w_0 = 4$. The faster (2-ps) lifetime corresponds to OD hydroxyls that are hydrogen bonded to the oxygens of water molecules while the second, slower lifetime is attributed to ODs bound to the sulfonate head groups. Unlike the larger reverse micelles, the value of the second, longer lifetime exhibits a frequency dependence. As the frequency of obser-

vation is increased, the population of the 2-ps lifetime decreases, and the population and the value of the slower lifetime increase. At the highest frequencies for AOT $w_0 = 2$, the population decay becomes a single slow exponential because essentially all of the signal comes from ODs that are bound to head groups. The two-component behavior arises because the vibrational lifetime is extremely sensitive to local environments. The water molecule hydroxyls in the small reverse micelles are mostly hydrogen bonded to the interface, but they can also form hydrogen bonds to the oxygens of other water molecules. These water–hydroxyl interactions give rise to the faster lifetime while water–interface interactions give rise to the slower lifetime. As the frequency is tuned to the blue, the nature of the OD–head group interactions change, which is reflected in a lifetime that steadily increases as the frequency increases.

The systems discussed above, AOT and Igepal reverse micelles, AOT lamellae, and water–salt solutions, all have sufficient water in the systems so that there is bulklike water in addition to water interacting with an interface or ion. Thus, water dynamics are of two types, bulk water and interfacial water. In a reverse micelle, such as AOT, and in other systems, the situation changes as the size of the water nanopool becomes small. In AOT reverse micelles it was found that there are three regimes of water nanopools–large, intermediate, and small [68]. The large reverse micelles have cores (a substantial amount of water well separated from the interface) with bulk water characteristics.

As the size of the water nanopool becomes smaller, a larger fraction of the water molecules interacts with the interface. The influence of the interface propagates out over some distance. In the intermediate regime, the nanopool is small enough that the influence of the interface has not completely died away at the center of the nanopool. This type of system has a core of water molecules, but the core does not have bulklike properties. In connection with Figure 1.14, it was found that w_0 values of 46, 37, 25, 16.5, and 12 all had interfacial water orientational relaxation times of 18 ps and core relaxation times with the bulk water value of 2.6 ps. Intermediate size reverse micelles, $w_0 = 10$ and $w_0 = 7.5$, have both interfacial and core orientational relaxation times and lifetimes that are somewhat longer than those observed for the large reverse micelles.

In the $w_0 = 2$ reverse micelle (see spectrum in Fig. 1.11), there are only two water molecules per AOT molecule. Hauser et. al [98], using differential scanning calorimetry, nuclear magnetic resonance (NMR), and electron spin resonance (ESR) experiments suggest that between four and six water molecules are required to hydrate the sulfonate head group of AOT. Although there may not be a bulk water-like core, HOD molecules in small reverse micelles have their ODs experiencing a variety of environments as demonstrated by a wavelength dependence to the vibrational lifetime [63].

While small variations in the local environment of a water molecule may affect the vibrational lifetime, the long-time orientational dynamics are related to the complete structural rearrangement of the hydrogen bonding network due to hydrogen bond switching events. Anisotropy decays for HOD in $w_0 = 2$ reverse micelles are shown in Figure 1.22 with the anisotropy decay of bulk water for comparison. In the $w_0 = 2$ reverse micelles, the sample has very little water, which results in

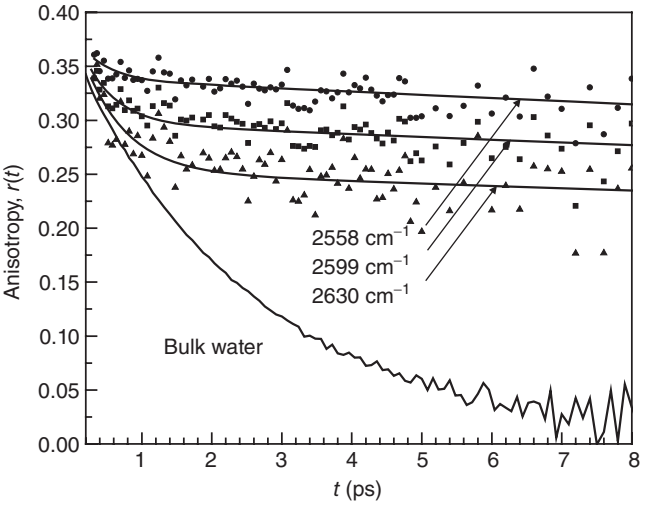

Figure 1.22 Anisotropy curves for AOT $w_0 = 2$ at three detection frequencies. There is very little anisotropy decay on this time scale, as compared to the anisotropy decay for bulk water. Anisotropy decay for the small reverse micelles is modeled by a wobbling-in-a-cone mechanism instead of the two-component anisotropy.

decreased signal-to-noise ratio. Nonetheless, the data are adequate to draw conclusions. After a very fast initial decay, the anisotropy decay in the reverse micelle has a very slow long-time decay. The long-time decays at a variety of wavelengths are identical within experimental error [68]. This behavior is consistent with the extremely low water content, only ~50 water molecules per reverse micelle for $w_0 = 2$. Essentially, hydrogen bond rearrangement is dramatically slowed because of the energetic penalty required to disrupt the structure of sulfonate groups, water molecules, and sodium ions at the interface.

The long-time orientational dynamics are independent of frequency because hydrogen bond switching is a concerted process that depends on new hydrogen bond acceptors moving into the first solvation shell of the reorienting water (see Figure 1.17), not the strength of a particular hydrogen bond [66, 67]. In a $w_0 = 2$ reverse micelle the hydrogen bonding network is completely coupled because so few water molecules are present. Therefore, the long-time orientational dynamics are well described by a single ensemble, not a core subensemble and an interface subensemble. The long-time anisotropy decays for all frequencies in the $w_0 = 2$ reverse micelle can be fit with the same time constant of 110 ± 40 ps. The large error bars indicate the uncertainty in determining such a long-time constant from a limited time range of data. It is interesting to note that the reorientation of water in the $w_0 = 2$ reverse micelle is still an order of magnitude faster than the tumbling time of the reverse micelle itself [99], indicating that water is still able to reorient albeit slowly.

The fast anisotropy decay component seen in Figure 1.22 is not due to a fraction of the water molecules that are completely reorienting on a time scale faster than

bulk water. Rather it is caused by local orientational motions of water molecules within a stable hydrogen bonding configuration. This type of restricted, incomplete orientational relaxation is referred to as wobbling in a cone [68, 93, 100]. It is associated with the wobbling of the orientation of the water molecules over a limited range of angles within an very slowly evolving hydrogen bonding network [68].

The concerted nature of water hydrogen bond rearrangement is responsible for the transition from two-component dynamics (large- and medium-sized water nanopools) to collective dynamics (very small water nanopools). As discussed above, Laage and Hynes showed that water reorientation occurs through a transition state that involves a bifurcated hydrogen bond that the rotating water molecule forms between the old and new hydrogen bond acceptors (see Fig. 1.17) [66, 67]. The new acceptor is originally in the second hydration shell of the rotating water molecule, but through concerted motions it moves into the first hydration shell, creating an overcoordinated environment for the rotating water molecule and reducing the energetic barrier for reorientation. This model shows that water reorientation is not a localized process; the reorientation of a single water molecule requires concerted rearrangement of both its first and second hydration shells involving ~16 water molecules [101]. If one or more of these 16 water molecules is itself in an environment that is not the same as bulk water, causing it to have dynamics distinct from bulk, it will affect the dynamics of its neighbors. When there are many unperturbed water molecules, such as in large reverse micelles, the effect of the perturbation dies off relatively quickly. However, in small reverse micelles, so many of the water molecules are perturbed that even water molecules not directly interacting with the interface have very slow dynamics.

1.7 SPECTRAL DIFFUSION MEASUREMENTS OF INTERFACIAL WATER DYNAMICS

1.7.1 Large and Intermediate AOT Reverse Micelles

The linear IR absorption and pump–probe data for larger reverse micelles all suggest that when the reverse micelles are large enough, two distinct environmental regions yield separable dynamics. Additional information can be obtained from measurements of spectral diffusion using 2D IR vibrational echo experiments. As representative 2D IR data for large reverse micelles, 2D IR spectra for AOT $w_0 = 16.5$ at three T_w's are shown in the left column of Figure 1.23 [102]. In the spectra, the peak along the diagonal is positive going and corresponds to the 0–1 vibrational transition while the off-diagonal peak is negative going and arises from vibrational echo emission at the 1–2 transition frequency. The 1–2 peak appears off the diagonal and shifted along the ω_m axis due to the vibrational anharmonicity. At early T_w values, the spectra are elongated along the diagonal, indicating that an oscillator excited at a certain frequency has a high probability of retaining that frequency after a short amount of time. The spectra become more symmetric as T_w lengthens and the hydroxyl stretches of the water molecules evolve in frequency due to structural evolution of the system.

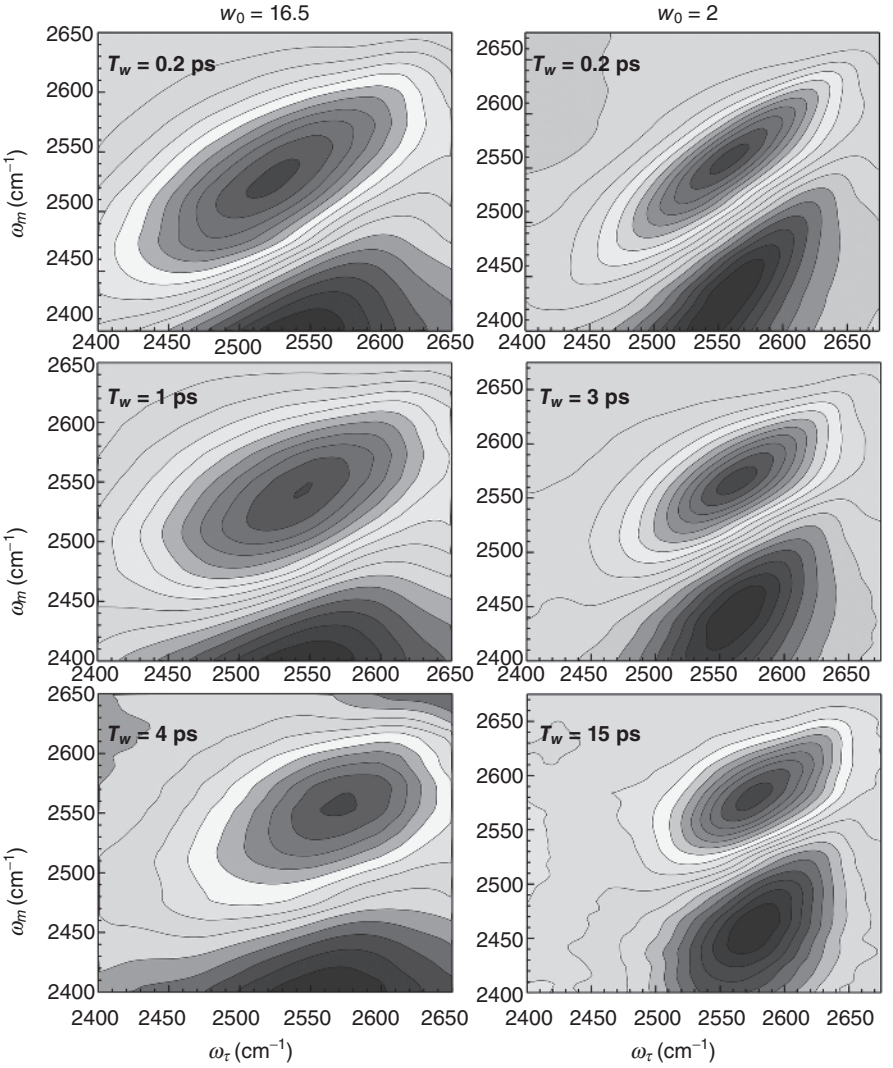

Figure 1.23 Two-dimensional IR vibrational echo correlation plots for AOT $w_0 = 16.5$ (left column) and AOT $w_0 = 2$ (right column) at a range of T_w's. Both samples show significant elongation along the diagonal at early time, and while $w_0 = 16.5$ shows faster spectral diffusion than $w_0 = 2$, neither sample completes spectral diffusion on the time scale of the experiment.

Figure 1.23 shows that the spectra maintain some elongation at long T_w. Therefore, spectral diffusion, which is caused by structural evolution, is not complete on the time scale of the experiment.

The large reverse micelles ($w_0 = 12$ and $w_0 = 16.5$) and intermediate reverse micelles ($w_0 = 7.5$) contain two types of water molecules: core water and interfacial water. In a 2D IR experiment, each of these ensembles generates a 2D IR spectrum

such that the measured 2D spectrum is a combination of the individual spectra. When the peak separation between components is relatively small, the individual spectra are not resolved.

As discussed in the introduction, the FFCF is obtained from 2D IR spectra via CLS analysis [84, 85]. Recently, a modified CLS technique was developed to account for two-component systems [81]. A 2D IR spectrum resulting from a two-component system can be decomposed into its constituent spectra, and each of these spectra has a characteristic CLS decay. In large reverse micelles, the components are bulk water, for which the CLS is already known from previous experiments [38, 39], and interfacial water. It is therefore possible to obtain the CLS decay (and by extension, the FFCF) of the interfacial water. It was found that for the two-component 2D IR spectrum (the combined spectrum) the peak positions (ω^*_{mC}) of slices parallel to the ω_m axis are weighted combinations of the peak positions (ω^*_{m1}) of the bulk water spectrum and the peak positions (ω^*_{m2}) of the second interfacial component:

$$\omega^*_{mC}(\omega_m, \omega_\tau, T_w) = f_1(\omega_\tau, T_w)\omega^*_{m1}(\omega_m, \omega_\tau, T_w) + [1 - f_1(\omega_\tau, T_w)]\omega^*_{m2}(\omega_m, \omega_\tau, T_w) \tag{1.14}$$

The set of peak positions for the slices are also known as centerline data. In Eq. (1.14), f_1 is the fractional population of bulk water, which is both T_w and frequency-dependent. This fraction term can be obtained from the FTIR absorption spectra of the two components and the measured vibrational lifetimes,

$$f_1(\omega_\tau, T_w) = \frac{S_1(\omega_\tau)e^{-T_w/T_1^{\mathrm{w}}}}{S_1(\omega_\tau)e^{-T_w/T_1^{\mathrm{w}}} + S_2(\omega_\tau)e^{-T_w/T_1^{\mathrm{int}}}} \tag{1.15}$$

where S_1 and S_2 are defined by Eq. (1.13). Eq. (1.14) can be rearranged to obtain ω^*_{m2} for the interface:

$$\omega^*_{m2}(\omega_m, \omega_\tau, T_w) = \frac{\omega^*_{m2C}(\omega_m, \omega_\tau, T_w) - f_1(\omega_\tau, T_w)\omega^*_{m1}(\omega_m, \omega_\tau, T_w)}{1 - f_1(\omega_\tau, T_w)} \tag{1.16}$$

For Eq. (1.16) to be employed, the f_1 fraction terms and vibrational lifetimes must be known. The peak position of the interfacial water absorption spectrum must also be known or reasonably approximated. When CLS analysis is applied to the calculated interfacial water centerline data, the CLS will be calculated around the peak position of the interfacial water band, which is 2565 cm^{-1} for $w_0 = 2$.

Centerline data for the interface, obtained by applying Eq. (1.16), were obtained for AOT $w_0 = 16.5$, 12, and 7.5 at the measured T_w's [102]. Here, we treat $w_0 = 7.5$ as a large reverse micelle, but it will be discussed later whether that approximation is valid. The interfacial CLS curves for these three micelles are displayed in Figure 1.24. The interfacial CLS curves are similar for $w_0 = 12$ and $w_0 = 16.5$ within error. The lack of a size dependence for the large reverse micelles is consistent with a lack of size dependence for the interfacial orientational relaxation and the vibrational lifetime. The $w_0 = 7.5$ system is considerably smaller in size, and its interfacial CLS decays slower than the larger reverse micelles. It should be noted that the bulk water centerline data were used in the $w_0 = 7.5$ calculation, even though the experiments suggest that the core is not exactly bulk-water-like. The core of the $w_0 = 7.5$ reverse

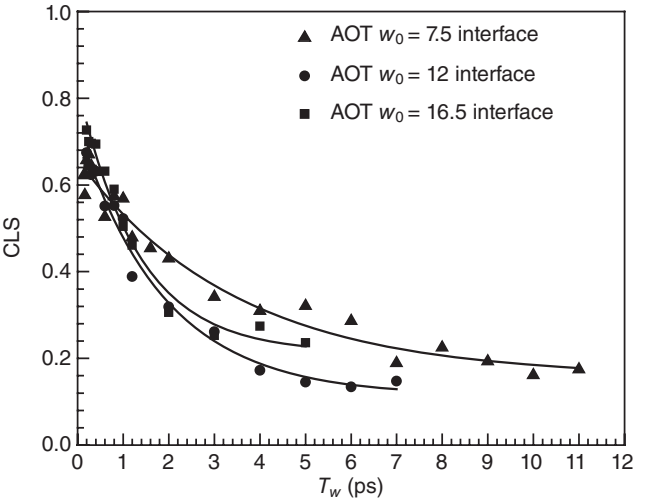

Figure 1.24 Interfacial CLS curves for large and intermediate reverse micelles. All curves decay as a single exponential to an offset. AOT $w_0 = 16.5$ and $w_0 = 12$ show very similar interfacial CLS curves, while AOT $w_0 = 7.5$ dynamics occur slightly slower. The curves through the data are the interfacial FFCFs for each sample.

Table 1.6 Interfacial FFCF Parameters for Large and Intermediate AOT Reverse Micelles[a]

w_0	Γ (cm^{-1})	Δ_1 (cm^{-1})	τ_1 (ps)	Δ_S (cm^{-1})
7.5	57	44	3.5	24
12	35	55	1.9	21
16.5	28	50	1.3	29

[a]Error bars are ±5 for Γ and Δ's; ±0.5 for τ_1.

micelle cannot be measured directly, so bulk water is the best approximation for use in the calculation.

The interfacial CLS curves fit well to a single exponential decay with a ~1.6-ps time constant plus an offset. The interfacial FFCFs for w_0 values of 16.5, 12, and 7.5 are listed in Table 1.6 and were calculated by simultaneously fitting the CLS curve and the $w_0 = 2$ spectrum for each sample. The $w_0 = 12$ and $w_0 = 16.5$ systems yield very similar FFCF parameters. Like the rotational and population relaxation dynamics, spectral diffusion at the interface in large reverse micelles is independent of size. This result implies that local water–interface interactions and dynamics do not change with size for sufficiently large reverse micelles.

The ~1.6-ps interfacial time constant is very similar to the 1.7-ps time constant in the FFCF for bulk water that corresponds to global hydrogen bond rearrangement. Water molecules at the interface are hydrogen bonded to the sulfonate head groups

but also to water molecules in the core region. The frequencies of the interfacial waters will be influenced by the motions and dynamics of the core. It is possible that the 1.6-ps decay arises from hydrogen bond rearrangement of noninterfacial waters that are making and breaking hydrogen bonds with the interfacial waters. If this proposition is correct, then water molecules immediately beyond the interfacial water layer must behave very much like bulk water. This conclusion supports the idea that an interface gives rise to a very localized strong perturbation of the water dynamics. The slower FFCF time constant of 3.5 ps for $w_0 = 7.5$ is in accord with the slowing down of core water in general in this sample, as seen by the observed retarded orientational dynamics in intermediate sizes.

The offset in the FFCFs (Δ_S terms in Table 1.6) corresponds to slow processes that cannot be measured within the experimental time window, which is limited by the vibrational lifetimes of the samples. Rotation at the interface has ~18 ps decay time, so it is likely that the offset includes effects from slow rotations. In addition, for spectral diffusion to be complete, the vibrational chromophores must sample all frequencies of the inhomogeneous line shape. This requirement means that interfacial water molecules need to exchange with core waters and diffuse to the core and vice versa. Exchange and diffusion will occur very slowly and contribute to the offset.

1.7.2 In Small AOT Reverse Micelles

The FFCFs for w_0 values of 2, 4, and 7.5 were determined by single-component CLS analysis [63]. Representative 2D IR spectra for $w_0 = 2$ are shown in the right column of Figure 1.23. Note the substantial difference between the 2D IR spectra of $w_0 = 2$ and $w_0 = 16.5$. The $w_0 = 2$ spectra are much more elongated along the diagonal at all times, and the evolution in shape is much slower than the $w_0 = 16.5$ spectra. The CLS curves for the three small AOT reverse micelles are shown in Figure 1.25. Orientational relaxation measurements for the $w_0 = 2$ and $w_0 = 4$ reverse micelles show that the structural dynamics behave essentially as a single ensemble. In the previous sections, $w_0 = 7.5$ was treated approximately using the two-component core–interface decomposition approach for the 2D IR spectral diffusion dynamics. Here $w_0 = 7.5$ is treated in the same manner as $w_0 = 2$ and $w_0 = 4$ for comparison. The experimental T_w range is limited by the vibrational lifetimes of each sample. Thus, data cannot be taken at the same T_w values for each sample.

The general trend of the CLS data is that spectral diffusion slows down as the water pool size decreases. The FFCF parameters determined for reverse micelles w_0 values of 2, 4, and 7.5 are listed in Table 1.7. The FFCF for a small reverse micelle takes the form of a biexponential decay with an offset and a motionally narrowed (homogeneous) component. All three FFCFs have a fast time constant of ~1 ps and a slower time constant of ~6–10 ps. Bulk water has a fast time constant of ~400 fs, which is attributed to fast local hydrogen bond fluctuations [89, 90]. Given the similarity in time scales and that the small reverse micelles represent very constrained environments, it is reasonable to propose that the ~1-ps time scale is also due to local hydrogen bond fluctuations. The static offset in the FFCF (not present in bulk

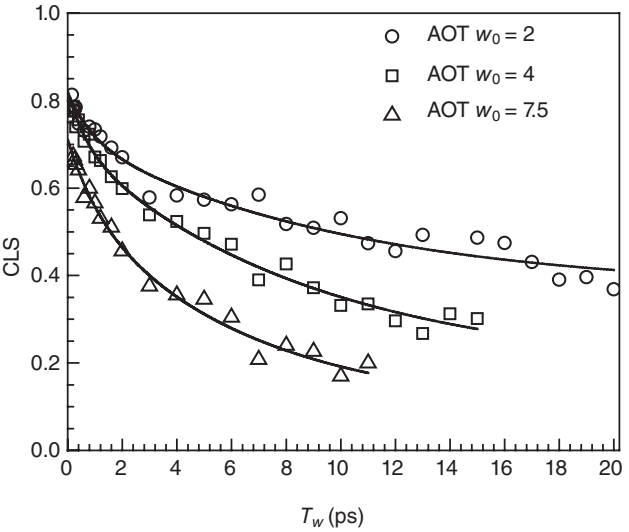

Figure 1.25 CLS curves for intermediate and small reverse micelles. These data have not been processed with the two-component CLS model. The lines through the data are the FFCFs for each sample. AOT $w_0 = 2$ shows the slowest decay.

Table 1.7 FFCF Parameters for Small and Intermediate AOT Reverse Micelles

w_0	Γ (cm^{-1})	Δ_1 (cm^{-1})	τ_1 (ps)	Δ_2 (cm^{-1})	τ_2 (ps)	Δ_S (cm^{-1})
2	33 ± 5	19 ± 2	0.9 ± 0.1	36 ± 1	10 ± 1	37 ± 1
4	33 ± 5	21 ± 2	0.7 ± 0.4	44 ± 5	8.9 ± 3	26 ± 1
7.5	57 ± 2	25 ± 2	1.1 ± 0.2	47 ± 3	6.4 ± 1	20 ± 2

water) arises from the extremely slow motions of the water molecules in the small reverse micelles. For spectral diffusion to be complete in any system (including both large and small reverse micelles), all water molecules must experience all environments. Rotations, diffusion through the reverse micelles, and exchange of populations between an OD hydroxyl bound to the interface and one bound to another water oxygen will occur very slowly in the highly confined environments of small reverse micelles.

It is possible that the intermediate 6 to 10-ps decay time scale is caused by hydrogen bond rearrangement of water molecules bound to the water directly at the interface with ones that have at least one or possibly both hydroxyls not bound to the interface. For the large reverse micelles, this mechanism was proposed because of the similarity of times for the interfacial and bulk water spectral diffusion. For the small reverse micelles the dynamics become increasingly slow as the diameter decreases. It is also possible that topography roughness of the surfactant head group

interface contributes to inhomogeneous broadening, and the motions of the head groups contribute to spectral diffusion of the water molecules. MD simulations have shown the necessity of including topography roughness in order to capture accurate line shapes [103].

In addition to the time constants, the FFCF also contains frequency fluctuation amplitudes (Δ terms) and a motionally narrowed component. Each time scale, including the static offset, produces a significant amount of inhomogeneous broadening. The motionally narrowed component (Γ) is roughly the same for $w_0 = 2$ and $w_0 = 4$, but is significantly greater for $w_0 = 7.5$. It needs to be noted that $w_0 = 7.5$ is not strictly a small reverse micelle and that neither FFCF model (large or small reverse micelle) is entirely correct. The $w_0 = 7.5$ system is quite different from $w_0 = 2$ and $w_0 = 4$ in that it has a distinct core. However, that core is not bulklike, so the bulk approximation in the previous section no doubt produces some error.

1.8 CONCLUDING REMARKS

Ultrafast IR spectroscopy is used here to probe the population relaxation, orientational relaxation, and spectral diffusion dynamics of water molecules near charged and neutral reverse micelle surfaces. Using polarization-selective pump–probe and 2D IR techniques, water dynamics are monitored on the picosecond time scale on which they are occurring. Furthermore, these experimental techniques use the actual water molecules (5% HOD in H_2O) in the system as probes and therefore measure the water dynamics directly, as opposed to using other probe molecules such as fluorescent dyes. Water, both as a bulk liquid and confined in reverse micelles, has a broad absorption band, indicating a large range of heterogeneity in the hydrogen bonding environments. Water molecules near the reverse micelle interface absorb more on the blue (high-frequency) side of the line shape, a property that greatly facilitates isolating interfacial water dynamics from bulk dynamics. One of the significant results discussed here is that IR spectral analysis, population relaxation, orientational dynamics (anisotropy), and spectral diffusion all follow a two-component model in large reverse micelles such that interfacial water has very distinct and separable dynamics from the bulk water core.

Population and reorientation relaxation results show that in AOT reverse micelles (charged sulfonate head groups) that are equal to or larger than $w_0 = 12$, the dynamics of the interface remain constant with water pool size and wavelength; only the fractional populations of the core and interface change with wavelength. The decay constants for vibrational relaxation and reorientation at the interface are 4.3 and 18 ps, respectively. The equivalent parameters in bulk water are 1.8 and 2.6 ps, respectively. The interface significantly retards water dynamics, but it does not immobilize the water molecules. Spectral diffusion at the interface has a decay time constant of ~1.6 ps that goes to a long-time scale offset. The offset arises from dynamical processes at the interface that are too slow to measure within the experimental time window. The 1.6-ps time constant is the same within experimental error to the slowest component of bulk water spectral diffusion (1.7 ps), suggesting that

water molecules at the interface are influenced by water molecules immediately beyond the interfacial layer in the core and that the effects of the interface are highly localized. The results suggest that water molecules just beyond the interfacial layer exhibit dynamics very similar to those of bulk water.

The results show that the presence of an interface substantially slows the hydrogen bond dynamics that are necessary for water to undergo structural evolution. An important issue is how important is the charge and chemical nature of the interface compared to just the presence of an interface of any type. In comparing the interfacial orientational relaxation at the AOT charged interface versus the Igepal neutral interface, it was found that there is at most a modest decrease in reorientation time for interfacial water molecules in Igepal reverse micelles. These results indicate that the presence of the interface is more important than its charge or chemical composition. As shown by 2D IR chemical exchange experiments on water–$NaBF_4$ solutions, the exchange time for a water hydroxyl bound to an anion to switch hydrogen bonds to another water hydroxyl is ~7 ps, which is only about a factor of 3 or 4 slower than the time for water–water hydrogen bond exchange in bulk water. This exchange behavior supports the observed small differences in interfacial water dynamics in AOT and Igepal reverse micelles.

Another question is whether the geometry of the nanoconfined system plays a role in water dynamics. Comparisons of interfacial water dynamics in large AOT reverse micelles and AOT lamellar structures demonstrates that the overall population and orientational relaxation times (4.3 and 18 ps, respectively) are the same for the two geometries. The dynamics are more similar for reverse micelles and lamellar structures of the same hydration level rather than for reverse micelles and lamellar structures of the same nanoscopic dimension (reverse micelle diameter or lamellar interplane separation). This observation further supports the conclusion that the interface only causes a strong perturbation of water dynamics in the immediate proximity of the interface.

As the reverse micelles become smaller, the water molecules start to feel the effects of nanoconfinement rather than only being influenced in the immediate presence of an interface. Intermediate sizes, such as AOT $w_0 = 10$ and $w_0 = 7.5$ show two-component behavior, but each region has slower dynamics than their counterparts in larger sizes. At very small sizes, such as $w_0 = 4$ and $w_0 = 2$, nearly all the water molecules interact with the interface and reorientation dynamics slow dramatically. The dynamics throughout the very small water pools are strongly influenced by the interface and behave more or less as a single ensemble with regard to hydrogen bond structural evolution.

The interplay between surfactant head group chemical identity, hydration level, water pool diameter, and geometry of the interface on interfacial water dynamics is complex in nature, but ultrafast IR spectroscopy has been able to provide detailed insights into the effects of these factors. Overall, slow water dynamics at the interface emerge as a very local effect that does not extend far beyond the first hydration layer for large systems in which the interfacial water is in contact with bulk water. However, when the distance scale of nanoconfinement becomes small, less than a couple of nanometers, the role of the interface changes. For very small nanoscopic

pool of water molecules, the interface controls the dynamics of the entire ensemble of water molecules.

ACKNOWLEDGMENTS

We would like to thank several individuals who participated in many of the experiments presented in this work. We would like to acknowledge Dr. David Moilanen, Daryl Wong, and Chiara Giammanco for their contributions. E.E.F. thanks the Stanford Graduate Fellowship Program for a research fellowship.

REFERENCES

1. Bagchi, B. Water dynamics in the hydration layer around proteins and micelles, *Chem. Rev.* **2005**, *105*, 3197.
2. Lum, K.; Chandler, D.; Weeks, J. D. Hydrophobicity at small and large length scales, *J. Phys. Chem. B* **1999**, *103*, 4570.
3. Wood, T. D.; Chorush, R. A.; Wampler, F. M.; Little, D. P.; O'Connor, P. B.; McLafferty, F. W. Gas-phase folding and unfolding of cytochrome-c cations, *Proc. Natl. Acad. Sci. U.S.A.* **1995**, *92*, 2451.
4. Levy, Y.; Onuchic, J. N. Water mediation in protein folding and molecular recognition, *Annu. Rev. Biophys. Biomol. Struct.* **2006**, *35*, 389.
5. Rose, G. D.; Wolfenden, R. Hydrogen bonding, hydrophobicity, packing, and protein folding, *Annu. Rev. Biophys. Biomol. Struct.* **1993**, *22*, 381.
6. Rhee, Y. M.; Sorin, E. J.; Jayachandran, G.; Lindahl, E.; Pande, V. S. Simulations of the role of water in the protein-folding mechanism, *Proc. Natl. Acad. Sci. U.S.A.* **2004**, *101*, 6456.
7. Helferrich, F. *Ion Exchange*, McGraw-Hill: New York, **1962**.
8. Zagorodni, A. A. *Ion Exchange Materials: Properties and Applications*, Elsevier: Oxford, **2007**.
9. Narayan, S.; Muldoon, J.; Finn, M. G.; Fokin, V. V.; Kolb, H. C.; Sharpless, K. B. "On water": Unique reactivity of organic compounds in aqueous suspension, *Angew. Chem. Int. Ed.* **2005**, *44*, 3275.
10. Jung, Y.; Marcus, R. A. On the theory of organic catalysis on water, *J. Am. Chem. Soc.* **2007**, *129*, 5492.
11. Jung, Y.; Marcus, R. A. Protruding interfacial OH groups and "on-water" heterogeneous catalysis, *J. Phys.: Condens. Matter* **2010**, *22*, 284117.
12. Hubbard, A. T. Electrochemistry at well-characterized surfaces, *Chem. Rev.* **1988**, *88*, 633.
13. Brown, G. E.; Henrich, V. E.; Casey, W. H.; Clark, D. L.; Eggleston, C.; Felmy, A.; Goodman, D. W.; Gratzel, M.; Maciel, G.; McCarthy, M. I.; Nealson, K. H.; Sverjensky, D. A.; Toney, M. F.; Zachara, J. M. Metal oxide surfaces and their interactions with aqueous solutions and microbial organisms, *Chem. Rev.* **1999**, *99*, 77.
14. Morse, J. W.; Arvidson, R. S.; Luttge, A. Calcium carbonate formation and dissolution, *Chem. Rev.* **2007**, *107*, 342.
15. Jungwirth, P.; Tobias, D. J. Specific ion effects at the air/water interface, *Chem. Rev.* **2006**, *106*, 1259.
16. Benjamin, I. Chemical reactions and solvation at liquid interfaces: A microscopic perspective, *Chem. Rev.* **1996**, *96*, 1449.
17. Newton, M. D.; Friedman, H. L. A proposed neutron-diffraction experiment to measure hydrogen isotope fractionation in solution, *J. Chem. Phys.* **1985**, *83*, 5210.
18. Mancinelli, R.; Botti, A.; Bruni, F.; Ricci, M. A.; Soper, A. K. Hydration of sodium, potassium, and chloride ions in solution and the concept of structure maker/breaker, *J. Phys. Chem. B* **2007**, *111*, 13570.

19. Collins, K. D.; Neilson, G. W.; Enderby, J. E. Ions in water: Characterizing the forces that control chemical processes and biological structure, *Biophys. Chem.* **2007**, *128*, 95.
20. Smith, J. D.; Saykally, R. J.; Geissler, P. L. The effect of dissolved halide anions on hydrogen bonding in liquid water, *J. Am. Chem. Soc.* **2007**, *129*, 13847.
21. Bakker, H. J.; Kropman, M. F.; Omata, Y.; Woutersen, S. Hydrogen-bond dynamics of water in ionic solutions, *Phys. Scr.* **2004**, *69*, C14.
22. Kropman, M. F.; Bakker, H. J. Dynamics of water molecules in aqueous solvation shells, *Science* **2001**, *291*, 2118.
23. Park, S.; Fayer, M. D. Hydrogen bond dynamics in aqueous NaBr solutions, *Proc. Natl. Acad. Sci. U.S.A.* **2007**, *104*, 16731.
24. Park, S.; Moilanen, D. E.; Fayer, M. D. Water dynamics–the effects of ions and nanoconfinement, *J. Phys. Chem. B* **2008**, *112*, 5279.
25. Moilanen, D. E.; Wong, D.; Rosenfeld, D. E.; Fenn, E. E.; Fayer, M. D. Ion-water hydrogen-bond switching observed with 2D IR vibrational echo chemical exchange spectroscopy, *Proc. Natl. Acad. Sci. U.S.A.* **2009**, *106*, 375.
26. Minbiao, J.; Odelius, M.; Gaffney, K. J. Large angular jump mechanism observed for hydrogen bond exchange in aqueous perchlorate solution, *Science* **2010**, *328*.
27. Brink, G.; Falk, M. Infrared spectrum of HDO in aqeous solutions of perchlorates and tetrafluoroborates, *Can. J. Chem.* **1970**, *48*, 3019.
28. Hopkins, A. J.; Schroedle, S.; Richmond, G. L. Specific ion effects of salt solutions at the CaF2/water interface, *Langmuir* **2010**, *26*, 10784.
29. Smith, J. D.; Cappa, C. D.; Messer, B. M.; Drisdell, W. S.; Cohen, R. C.; Saykally, R. J. Probing the local structure of liquid water by x-ray absorption spectroscopy, *J. Phys. Chem. B* **2006**, *110*, 20038.
30. Kerisit, S.; Rosso, K. M. Transition path sampling of water exchange rates and mechanisms around aqueous ions, *J. Chem. Phys.* **2009**, *131*.
31. Dzombak, D. A.; Hudson, R. J. M. Ion exchange: The contributions of diffuse layer sorption and surface complexation, in *Advances in Chemistry Series; Aquatic Chemistry: Interfacial and Interspecies Processes*, C. P. Huang, C. R. O'Melia, and J. J. Morgan, eds., Washington, DC, **1995**, Vol. *244*, p. 59.
32. Lin, Y. S.; Auer, B. M.; Skinner, J. L. Water structure, dynamics, and vibrational spectroscopy in sodium bromide solutions, *J. Chem. Phys.* **2009**, *131*, 144511.
33. Argyris, D.; Cole, D. R.; Striolo, A. Ion-specific effects under confinement: the role of interfacial water, *ACS Nano* **2010**, *4*, 2035.
34. Joung, I. S.; Cheatham, T. E., III. Molecular dynamics simulations of the dynamic and energetic properties of alkali and halide ions using water-model-specific ion parameters, *J. Phys. Chem. B* **2009**, *113*.
35. Lyubartsev, A. P.; Laaksonen, A. Concentration effects in aqueous NaCl solutions. A molecular dynamics simulation, *J. Phys. Chem.* **1996**, *100*, 16410.
36. Fecko, C. J.; Eaves, J. D.; Loparo, J. J.; Tokmakoff, A.; Geissler, P. L. Ultrafast hydrogen-bond dynamics in the infrared spectroscopy of water, *Science* **2003**, *301*, 1698.
37. Fecko, C. J.; Loparo, J. J.; Roberts, S. T.; Tokmakoff, A. Local hydrogen bonding dynamics and collective reorganization in water: Ultrafast infrared spectroscopy of HOD/D_2O, *J. Chem. Phys.* **2005**, *122*, 054506.
38. Asbury, J. B.; Steinel, T.; Kwak, K.; Corcelli, S. A.; Lawrence, C. P.; Skinner, J. L.; Fayer, M. D. Dynamics of water probed with vibrational echo correlation spectroscopy, *J. Chem. Phys.* **2004**, *121*, 12431.
39. Asbury, J. B.; Steinel, T.; Stromberg, C.; Corcelli, S. A.; Lawrence, C. P.; Skinner, J. L.; Fayer, M. D. Water dynamics: Vibrational echo correlation spectroscopy and comparison to molecular dynamics simulations, *J. Phys.Chem. A* **2004**, *108*, 1107.
40. Nicodemus, R. A.; Ramasesha, K.; Roberts, S. T.; Tokmakoff, A. Hydrogen bond rearrangements in water probed with temperature-dependent 2D IR, *J. Phys. Chem. Lett.* **2010**, *1*, 1068.
41. Cowan, M. L.; Bruner, B. D.; Huse, N.; Dwyer, J. R.; Chugh, B.; Nibbering, E. T. J.; Elsaesser, T.; Miller, R. J. D. Ultrafast memory loss and energy redistribution in the hydrogen bond network of liquid H_2O, *Nature* **2005**, *434*, 199.

42. Loparo, J. J.; Roberts, S. T.; Tokmakoff, A. Multidimensional infrared spectroscopy of water. I. Vibrational dynamics in two-dimensional IR line shapes, *J. Chem. Phys.* **2006**, *125*, 194521.
43. Loparo, J. J.; Roberts, S. T.; Tokmakoff, A. Multidimensional infrared spectroscopy of water. II. Hydrogen bond switching dynamics, *J. Chem. Phys.* **2006**, *125*, 194522.
44. Ganim, Z.; Jones, K. C.; Tokmakoff, A. Insulin dimer dissociation and unfolding revealed by amide I two-dimensional infrared spectroscopy, *Phys. Chem. Chem. Phys.* **2010**, *12*, 3579.
45. Finkelstein, I. J.; Zheng, J.; Ishikawa, H.; Kim, S.; Kwak, K.; Fayer, M. D. Probing dynamics of complex molecular systems with ultrafast 2D IR vibrational echo spectroscopy, *Phys. Chem. Chem. Phys.* **2007**, *9*, 1533.
46. DeFlores, L. P.; Ganim, Z.; Ackley, S. F.; Chung, H. S.; Tokmakoff, A. The anharmonic vibrational potential and relaxation pathways of the amide I and II modes of N-methylacetamide, *J. Phys. Chem. B.* **2006**, *110*, 18973.
47. Mukherjee, P.; Kass, I.; Arkin, I. T.; Zanni, M. T. Picosecond dynamics of a membrane protein revealed by 2D IR, *Proc. Natl. Acad. Sci. U.S.A.* **2006**, *103*, 3528.
48. Ishikawa, H.; Kwak, K.; Chung, J. K.; Kim, S.; Fayer, M. D. Direct observation of fast protein conformational switching, *Proc. Natl. Acad. Sci. U.S.A.* **2008**, *105*, 8619.
49. Tucker, M. J.; Gai, X. S.; Fenlon, E. E.; Brewer, S. H.; Hochstrasser, R. M. 2D IR photon echo of azido-probes for biomolecular dynamics, *Phys. Chem. Chem. Phys.* **2011**, *13*, 2237.
50. Chung, J. K.; Thielges, M. C.; Bowman, S. J.; Bren, K. L.; Fayer, M. D. Temperature dependent equilibrium native to unfolded protein dynamics and properties observed with IR absorption and 2D IR vibrational echo experiments, *J. Am. Chem. Soc.* **2011**, *133*, 6681.
51. Chung, J. K.; Thielges, M. C.; Fayer, M. D. Dynamics of the folded and unfolded villin headpiece (HP35) measured with ultrafast 2D IR vibrational echo spectroscopy, *Proc. Natl. Acad. Sci. U.S.A.* **2011**, *108*, 3578.
52. Thielges, M. C.; Chung, J. K.; Fayer, M. D. Protein dynamics in cytochrome P450 molecular recognition and substrate specificity using 2D IR vibrational echo spectroscopy, *J. Am. Chem. Soc.* **2011**, *133*, 3995.
53. Rosenfeld, D. E.; Kwak, K.; Gengeliczki, Z.; Fayer, M. D. Hydrogen bond migration between molecular sites observed with ultrafast 2D IR chemical exchange spectroscopy, *J. Phys. Chem. B* **2010**, *114*, 2383.
54. Kim, Y. S.; Hochstrasser, R. M. Chemical exchange 2D IR of hydrogen-bond making and breaking, *Proc. Natl. Acad. Sci. U.S.A.* **2005**, *102*, 11185.
55. Zheng, J.; Kwak, K.; Asbury, J. B.; Chen, X.; Piletic, I. R.; Fayer, M. D. Ultrafast dynamics of solute-solvent complexation observed at thermal equilibrium in real time, *Science* **2005**, *309*, 1338.
56. Zheng, J.; Kwak, K.; Xie, J.; Fayer, M. D. Ultrafast carbon-carbon single bond rotational isomerization in room temperature solution, *Science* **2006**, *313*, 1951.
57. Kwak, K.; Zheng, J.; Cang, H.; Fayer, M. D. Ultrafast 2D IR vibrational echo chemical exchange experiments and theory, *J. Phys. Chem. B.* **2006**, *110*, 19998.
58. Zulauf, M.; Eicke, H. F. Inverted micelles and microemulsions in the ternary-system H_2O-aerosol-OT-isooctane as studied by photon correlation spectroscopy, *J. Phys. Chem.* **1979**, *83*, 480.
59. Kinugasa, T.; Kondo, A.; Nishimura, S.; Miyauchi, Y.; Nishii, Y.; Watanabe, K.; Takeuchi, H. Estimation for size of reverse micelles formed by AOT and SDEHP based on viscosity measurement, *Coll. Surf. A—Physicochem. Eng. Aspects* **2002**, *204*, 193.
60. Eicke, H.-F.; Rehak, J. On the formation of water/oil-microemulsions, *Helv. Chim. Acta* **1976**, *59*, 2883.
61. Piletic, I. R.; Moilanen, D. E.; Spry, D. B.; Levinger, N. E.; Fayer, M. D. Testing the core/shell model of nanoconfined water in reverse micelles using linear and nonlinear IR spectroscopy, *J. Phys. Chem. A* **2006**, *110*, 4985.
62. Izquierdo, C.; Moya, M. L.; Usero, J. L.; Casado, J. Estimation of the aggregation number and core radius of microemulsions, *Monatsh. Chem.* **1992**, *123*, 383
63. Fenn, E. E.; Wong, D. B.; Fayer, M. D. Water dynamics in small reverse micelles in two solvents: Two-dimensional infrared vibrational echoes with two-dimensional background subtraction, *J. Chem. Phys.* **2011**, *134*, 054512.

64. Kenkre, V. M.; Tokmakoff, A.; Fayer, M. D. Theory of vibrational relaxation of polyatomic molecules in liquids, *J. Chem. Phys.* **1994**, *101*, 10618.
65. Egorov, S. A.; Berne, B. J. Vibrational energy relaxation in the condensed phases: quantum vs. classical bath for multiphonon processes, *J. Chem. Phys.* **1997**, *107*, 6050.
66. Laage, D.; Hynes, J. T. On the molecular mechanism of water reorientation, *J. Phys. Chem. B* **2008**, *112*, 14230.
67. Laage, D.; Hynes, J. T. A molecular jump mechanism of water reorientation, *Science* **2006**, *311*, 832.
68. Moilanen, D. E.; Fenn, E. E.; Wong, D.; Fayer, M. D. Water dynamics in large and small reverse micelles: from two ensembles to collective behavior, *J. Chem. Phys.* **2009**, *131*, 014704.
69. Moilanen, D. E.; Fenn, E. E.; Wong, D.; Fayer, M. D. Water dynamics in AOT lamellar structures and reverse micelles: Geometry and length scales vs. surface interactions, *J. Am. Chem. Soc.* **2009**, *131*, 8318.
70. Moilanen, D. E.; Fenn, E. E.; Wong, D.; Fayer, M. D. Water dynamics at the interface in AOT reverse micelles, *J. Phys. Chem. B* **2009**, *113*, 8560.
71. Fenn, E. E.; Wong, D. B.; Fayer, M. D. Water dynamics at neutral and ionic interfaces, *Proc. Natl. Acad. Sci. U.S.A.* **2009**, *106*, 15243.
72. Fenn, E. E.; Moilanen, D. E.; Levinger, N. E.; Fayer, M. D. Water dynamics and interactions in water-polyether binary mixtures, *J. Am. Chem. Soc.* **2009**, *131*, 5530.
73. Gaffney, K. J.; Piletic, I. R.; Fayer, M. D. Orientational relaxation and vibrational excitation transfer in methanol–carbon tetrachloride solutions, *J. Chem. Phys.* **2003**, *118*, 2270.
74. Woutersen, S.; Bakker, H. J. Resonant intermolecular transfer of vibrational energy in liquid water, *Nature (London)* **1999**, *402*, 507.
75. Corcelli, S.; Lawrence, C. P.; Skinner, J. L. Combined electronic structure/molecular dynamics approach for ultrafast infrared spectroscopy of dilute HOD in liquid H_2O and D_2O, *J. Chem. Phys.* **2004**, *120*, 8107.
76. Maitra, A. Determination of size parameters of water aerosol OT oil reverse micelles from their nuclear magnetic-resonance data, *J. Phys. Chem.* **1984**, *88*, 5122.
77. Kon-No, K.; Kitahara, A. Solubility behavior of water in nonaqueous solutions of oil-soluble surfactants—effect of molecular structure of surfactants and solvents, *J. Colloid Interface Sci.* **1971**, *37*, 469.
78. Lipgens, S.; Schubel, D.; Schlicht, L.; Spilgies, J.-H.; Ilgenfritz, G.; Eastoe, J.; Heenan, R. K. Percolation in nonionic water-in-oil-microemulsion systems: A small angle neutron scattering study, *Langmuir* **1998**, *14*, 1041.
79. Mukamel, S. *Principles of Nonlinear Optical Spectroscopy*, Oxford University Press: New York, **1995**.
80. Hamm, P.; Zanni, M. T. *Concepts and Methods of 2D Infrared Spectroscopy*, Cambridge University Press: Cambridge, **2011**.
81. Fenn, E. E.; Fayer, M. D. Extracting 2D IR frequency-frequency correlation functions from two component systems, *J. Chem. Phys.* **2011**, *135*, 074502.
82. Gruetzmacher, J. A.; Scherer, N. F. Few-cycle mid-infrared pulse generation, characterization, and coherent propagation in optically dense media, *Rev. Sci. Instrum.* **2002**, *73*, 2227.
83. Demirdoven, N.; Khalil, M.; Golonzka, O.; Tokmakoff, A. Dispersion compensation with optical materials for compression of intense sub-100-fs mid-infrared pulses, *Opt. Lett.* **2002**, *27*, 433.
84. Kwak, K.; Rosenfeld, D. E.; Fayer, M. D. Taking apart the two-dimensional infrared vibrational echo spectra: more information and elimination of distortions, *J. Chem. Phys.* **2008**, *128*, 204505.
85. Kwak, K.; Park, S.; Finkelstein, I. J.; Fayer, M. D. Frequency-frequency correlation functions and apodization in 2D-IR vibrational echo spectroscopy: A new approach, *J. Chem. Phys.* **2007**, *127*, 124503.
86. Saven, J. G.; Skinner, J. L. A molecular theory of the line shape—inhomogeneous and homogeneous electronic spectra of dilute chromophores in nonpolar fluids, *J. Chem. Phys.* **1993**, *99*, 4391.
87. Roberts, S. T.; Loparo, J. J.; Tokmakoff, A. Characterization of spectral diffusion from two-dimensional line shapes, *J. Chem. Phys.* **2006**, *125*, 084502.

88. Cho, M. H.; Yu, J. Y.; Joo, T. H.; Nagasawa, Y.; Passino, S. A.; Fleming, G. R. The integrated photon echo and solvation dynamics, *J. Phys. Chem.* **1996**, *100*, 11944.
89. Lawrence, C. P.; Skinner, J. L. Vibrational spectroscopy of HOD in liquid D_2O. III. Spectral diffusion, and hydrogen-bonding and rotational dynamics, *J. Chem. Phys.* **2003**, *118*, 264.
90. Corcelli, S. A.; Lawrence, C. P.; Asbury, J. B.; Steinel, T.; Fayer, M. D.; Skinner, J. L. Spectral diffusion in a fluctuating charge model of water, *J. Chem. Phys.* **2004**, *121*, 8897.
91. Tokmakoff, A. Orientational correlation functions and polarization selectivity for nonlinear spectroscopy of isotropic media. 1. third order, *J. Chem. Phys.* **1996**, *105*, 1.
92. Lipari, G.; Szabo, A. Effect of librational motion on fluorescence depolarization and nuclear magnetic-resonance relaxation in macromolecules and membranes, *Biophys. J.* **1980**, *30*, 489.
93. Wang, C. C.; Pecora, R. Time-correlation functions for restricted rotational diffusion, *J. Chem. Phys.* **1980**, *72*, 5333.
94. Kropman, M. F.; Bakker, H. J. Femtosecond mid-infrared spectroscopy of aqueous solvation shells, *J. Chem. Phys.* **2001**, *115*, 8942.
95. Collins, K. D. Charge density-dependent strength of hydration and biological structure, *Biophys. J.* **1997**, *72*, 65.
96. Rezus, Y. L. A.; Bakker, H. J. Orientational dynamics of isotopically diluted H_2O and D_2O, *J. Chem. Phys.* **2006**, *125*, 144512.
97. Fontell, K. The structure of the lamellar liquid crystalline phase in aerosol OT-water system, *J. Colloid Interface Sci.* **1973**, *44*, 318.
98. Hauser, H.; Haering, G.; Pande, A.; Luisi, P. L. Interaction of water with sodium Bis(2-ethyl-1-hexyl) sulfosuccinate in reversed micelles, *J. Phys. Chem.* **1989**, *93*, 7869.
99. Spry, D. B.; Goun, A.; Glusac, K.; Moilanen, D. E.; Fayer, M. D. Proton Transport and the water environment in nafion fuel cell membranes and AOT reverse micelles, *J. Am. Chem. Soc* **2007**, *129*, 8122.
100. Lipari, G.; Szabo, A. Model-free approach to the interpretation of nuclear magnetic-resonance relaxation in macromolecules 1. Theory and range of validity, *J. Am. Chem. Soc.* **1982**, *104*, 4546.
101. Yan, Z.; Buldyrev, S. V.; Kumar, P.; Giovambattista, N.; Debenedetti, P. G.; Stanley, H. E. Structure of the first- and second-neighbor shells of simulated water: Quantitative relation to translational and orientational order, *Phys. Rev. E: Stat., Nonlinear, Soft Matter Phys.* **2007**, *76*, 051201.
102. Fenn, E.E.; Wong, D.B.; Glammanco, C.H.; Fayer, M.D. Dynamics of water at the interface in reverse micelles: measurements of spectral diffusion with 2D IR vibrational echoes, *J. Phys. Chem. B* **2011**, *115*, 11658.
103. Pieniazek, P. A.; Lin, Y.-S.; Chowdhary, J.; Ladanyi, B. M.; Skinner, J. L. Vibrational spectroscopy and dynamics of water confined inside reverse micelles, *J. Phys. Chem. B* **2009**, *113*, 15017.